https://doi.org/10.5194/egusphere-2026-6639
Preprint. Discussion started: 30 October 2026
© Author(s) 2026. CC BY 4.0 License.

Virga hidden within the blind zone of spaceborne radars: implications for surface snowfall estimates in coastal East Antarctica

Giacomo Roversi[1,2], Alessandro Bracci[3], Hajime Okamoto[4], Kaori Sato[4], and Luca Baldini[2]

[1]Department of Environmental Sciences, Informatics and Statistics (DAIS), Ca' Foscari University of Venice, Venice, Italy
[2]Institute of Atmospheric Sciences and Climate, National Research Council (CNR-ISAC), Rome, Italy
[3]Institute of Atmospheric Sciences and Climate, National Research Council (CNR-ISAC), Bologna, Italy
[4]Research Institute for Applied Mechanics (RIAM), Kyushu University, Fukuoka, Japan

Correspondence: Giacomo Roversi (giacomo.roversi@unive.it)

Abstract. Antarctic snowfall is the main mass input to the Antarctic Ice Sheet, and its estimate relies mainly on satellite remote sensing. Unfortunately, because of ground clutter, the two W-band Cloud Profiling Radars (CPRs) on board CloudSat (NASA, 2006–2023) and EarthCARE (ESA–JAXA, 2024–ongoing) cannot reliably observe the lowest ∼1000 m and ∼500 m of atmosphere respectively ("blind zone"). Surface snowfall must then be estimated by assuming that what is detected aloft reaches the ground. But in katabatic-driven coastal East Antarctica this assumption is frequently violated by virga, precipitation that sublimates completely before reaching the surface. We analyse four years (2020–2021, 2023–2024) of vertical Doppler radar profiles (MRR-2, 24 GHz) and co-located optical disdrometer data at the Italian Mario Zucchelli Station. We identify *virga* profiles when hydrometeors detected aloft produce no signal at the lowest radar gate (105 m) or in the disdrometer. *Virga* accounts for 38 % of the hydrometeor-bearing columns. At the EarthCARE-like lowest observable heights, part of the virga becomes indistinguishable from precipitation and the four-year surface accumulation is overestimated by 29–30 % (up to 34 % switching to CloudSat). ERA5 reproduces the dry layer but still deposits snowfall in 90 % of the virga hours, accumulating on average 156 mm yr^{-1} against 53–106 mm yr^{-1} from the radar-based estimates. These results quantify the blind-zone impact at a coastal Antarctic site, sampling unprecedentedly close to the ground, and establish the ground-based classification, released as an open-source package, as a transferable constraint for satellite and reanalysis products.

1 Introduction

Snowfall is the dominant positive term of the surface mass balance of the Antarctic Ice Sheet (Palerme et al., 2014), and its variability directly modulates the ice-sheet contribution to sea level (IPCC, 2021). For mass-balance purposes, however, the relevant quantity is not the precipitation generated aloft, but the snow that actually reaches the surface. As shown in this study, the two can differ substantially in the lowest few hundred metres of the Antarctic atmosphere.

Measuring surface snowfall in Antarctica is difficult, and none of the instruments available at the ground is free of limitations in the harsh conditions of the continent. The ground instruments fall into a few families, each with its own failure mode: catching gauges that collect the falling snow, non-catching sensors that infer it from an energy balance, snow stakes and acoustic gauges that measure the depth accumulated at the ground, and optical disdrometers that observe the particles in the

https://doi.org/10.5194/egusphere-2026-6639
Preprint. Discussion started: 30 October 2026
© Author(s) 2026. CC BY 4.0 License.

air. Precipitation gauges, the standard reference at lower latitudes, are strongly affected by wind-induced undercatch. The intercomparison campaigns that established the transfer functions now in use show that the catch efficiency decreases steeply with wind speed and depends on air temperature, so that the corrections needed in cold and windy environments are large and remain site-dependent (Kochendorfer et al., 2017b; Nitu et al., 2018), and that a residual bias persists even when a wind shield is installed (Kochendorfer et al., 2017a). Weighing gauges also need heating and a stable power supply, which is demanding at unattended sites, although recent Antarctic deployments show that an autonomous installation is feasible (Seefeldt et al., 2021). The alternatives replace these problems with others: hot-plate sensors respond quickly but rely on an energy balance that the wind itself perturbs (Rasmussen et al., 2011; Zelasko et al., 2018), and acoustic depth gauges measure the snow that has accumulated rather than the snow that has fallen, so that erosion and redistribution by the wind enter the measurement together with the precipitation (Knuth et al., 2010). Optical disdrometers avoid the catchment problem altogether, because they observe the particles in the air rather than collecting them, and they estimate the diameter and the fall velocity of each particle crossing the sampling section. Their sampling efficiency is nevertheless lower than unity and decreases with wind speed, and they size irregular snowflakes ambiguously (Battaglia et al., 2010). Blowing snow then affects all of these instruments alike, because the particles lifted from the surface are counted as precipitation although they never fell from a cloud (Gossart et al., 2017). On top of these difficulties, the stations equipped for quantitative precipitation monitoring are few and concentrated along the coast, leaving the vast majority of the continent unsampled (Palerme et al., 2017). Continent-scale estimates therefore rely on atmospheric models and on satellite remote sensing.

Among the spaceborne sensors, radars are the only ones that resolve the vertical structure of precipitation (a lidar beam is extinguished in the first optically thick layer it meets). The CloudSat Cloud Profiling Radar (CPR) has provided the reference climatology of Antarctic snowfall (Milani et al., 2018; Souverijns et al., 2018), now continued, with Doppler capability, by the CPR on board EarthCARE (Wehr et al., 2023), which provides information on vertical air motions and particle fall speeds (Sato and Okamoto, 2025; Okamoto et al., 2025), and, in the coming years, by the WIVERN mission (Illingworth et al., 2018), selected as the eleventh ESA Earth Explorer. Spaceborne radar observations also anchor the passive microwave retrievals that extend the coverage of high-latitude snowfall estimates (Battaglia and Panegrossi, 2020; Camplani et al., 2024). The CloudSat surface snowfall product is the observational benchmark against which the reanalyses and the global precipitation data sets used in mass-balance studies are evaluated (Palerme et al., 2017; Song et al., 2026). These climatologies, from the first continental estimate of Palerme et al. (2014) onwards, rest on what the radar sees at its lowest usable gate.

Surface clutter, however, prevents the use of the range gates closest to the ground of any spaceborne radar for precipitation parameter estimation. Direct retrievals therefore apply only to heights of several hundred metres above the ground. Moreover, the depth of the affected layer is not fixed, but depends on the characteristics of the terrain, on the atmospheric conditions and the way the instrument's processing handles the contaminated gates (Palerme et al., 2019; Valdivia et al., 2022).

The layer between the surface and the lowest range gate unaffected by ground clutter is referred to as the blind zone (BZ). Within it the backscattered signal is dominated by the ground return, which severely limits the retrieval of the atmospheric parameters.

https://doi.org/10.5194/egusphere-2026-6639
Preprint. Discussion started: 30 October 2026
© Author(s) 2026. CC BY 4.0 License.

Estimating the snowfall at the surface from aloft therefore relies on an assumption about what happens below the lowest usable gate. The CloudSat snowfall algorithm (2C-SNOW-PROFILE) takes the snowfall rate at the surface to be the one retrieved in the lowest bin free from clutter, assuming that such precipitation will reach the ground unaltered, so that none of the processes acting below that height is represented (Palerme et al., 2019). The failure of this assumption over the polar regions was recognised early in the CloudSat era (Maahn et al., 2014).

In coastal East Antarctica this assumption often fails because of the low-level dynamics. Precipitation is delivered by synoptic systems and moisture intrusions of oceanic origin (Gorodetskaya et al., 2014; Jullien et al., 2020), while the boundary layer is dominated by the katabatic drainage of cold, dry air from the interior (Parish and Cassano, 2003). Terra Nova Bay is located in a confluence zone where the katabatic flow meets the moist maritime air of the Ross Sea and interacts with barrier winds along the Transantarctic Mountains (Argentini and Mastrantonio, 1994). The interplay of these flows produces a persistent dry sub-cloud layer in which falling snow can partially or entirely sublimate. Combining one year of observations on the coast of Adélie Land with simulations from different atmospheric models, Grazioli et al. (2017) estimated that this low-level sublimation reduces the total snowfall by 17 % over the continent and by up to 35 % on the margins of East Antarctica. The regional climate model MAR gives figures of the same order, with an atmospheric sublimation equal to 16 % of the snowfall reaching the grounded ice sheet in 2015, and to 26 % over the areas below 1000 m a.s.l. (Agosta et al., 2019). Those same margins receive most of the Antarctic snowfall (Bromwich et al., 2004), so the loss applies to the largest share of the continental accumulation.

Precipitation that evaporates or sublimates before reaching the ground is referred to as virga (American Meteorological Society, 2015). The phenomenon is not specific to the polar regions. At the global scale, the precipitation radars of TRMM and GPM, whose orbits are inclined by 35 and 65 degrees and therefore never reach the polar regions, find virga in more than 30 % of the columns they detect over the arid regions, while the CloudSat CPR reports about twice that occurrence (Wang et al., 2018). The difference between the two estimates comes from the different areas covered but also from the different sensitivity of the instruments. How much virga is detected depends on the observing system as well as on the atmosphere. In a vertically pointing radar, virga appears as a reflectivity that decreases below cloud base until the echo disappears. Micro Rain Radars (MRR) have documented it at mid-latitudes over the Swiss Plateau (Beynon and Hocke, 2022) and at several polar sites. In the Arctic, virga occurrence and precipitation phase have been related to the temperature and moisture of the advected air masses by MRR profiles at Ny-Ålesund (Saini et al., 2025, 2026a, b). In Antarctica, virga has been characterised at the French coastal research station Dumont d'Urville (DDU) (Durán-Alarcón et al., 2019; Wiener et al., 2024), where the katabatic outflow sustains the low-level sublimation (Grazioli et al., 2017), at the Belgian Princess Elisabeth research station, where a transect of profilers showed its occurrence varying with the local orography over a few tens of kilometres (Ferrone and Berne, 2023; Ferrone et al., 2023), and at Davis research station, where about 50 % of the snowfall mass was estimated to sublimate between the level of the snowfall peak, at 1.2 km, and 205 m, with virga associated with Föhn conditions in the lee of an ice ridgeline (Alexander et al., 2023). At the Italian Mario Zucchelli Station at Terra Nova Bay (MZS), combined MRR–disdrometer observations quantified the associated reduction of the snowfall rate in the lowest levels (Bracci et al., 2022a, b).

https://doi.org/10.5194/egusphere-2026-6639
Preprint. Discussion started: 30 October 2026
© Author(s) 2026. CC BY 4.0 License.

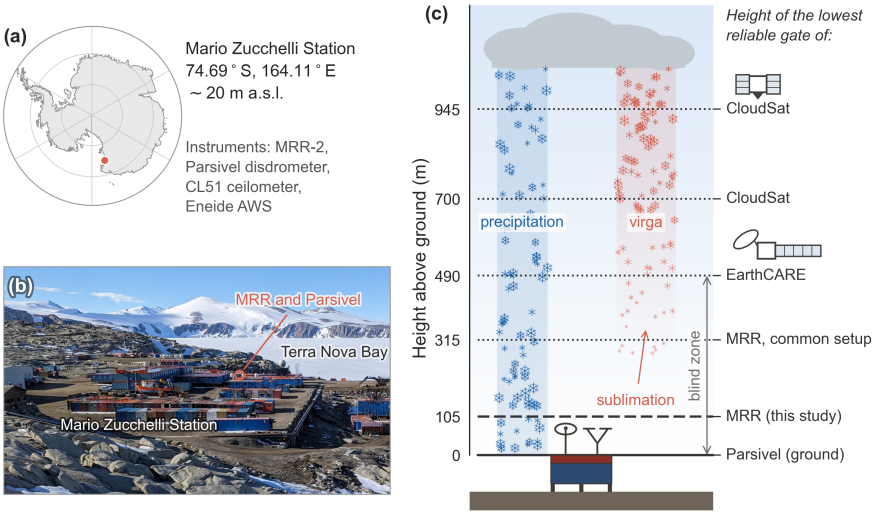

Figure 1. Overview of the site and of the observing geometry addressed in this study. (a) Location of Mario Zucchelli Station in Antarctica. (b) The station seen from the hills behind it, with the sea ice of Terra Nova Bay in the background (photo: G. Roversi). The circle marks the MRR and the disdrometer. (c) The lowest heights at which the different observing systems can still measure precipitation, from the disdrometer at the surface to the two lowest CloudSat range bins compared at this site by Bracci et al. (2023), 700 and 945 m. These heights are the nominal heights of the MRR range gates that stand in for each system, and their definition as lowest observable heights (LOH) is given in Sect. 2.3. The two shafts illustrate the two classes used throughout the paper, snow reaching the ground on the left and snow sublimating below cloud base on the right. The satellite icons mark the LOH of the two spaceborne configurations and are not meant to represent their observing beams. Only the height axis is quantitative, the rest of the panel is schematic. The two instruments are drawn on the roof of a station module, which is where they are installed.

What is still missing is a multi-year, event-independent quantification of (1) how often the precipitation detected aloft fails to reach the ground and (2) the resulting error on the surface accumulation estimated from blind-zone-limited observational geometries such as those of the CloudSat and EarthCARE CPRs. This quantification requires observations that extend well below the heights accessible to satellite radars, and that cover enough years for the result not to depend on the particular seasons sampled. Figure 1 places those heights on a single vertical axis, from the disdrometer at the surface up to the lowest levels the two CPRs can use, together with the two situations this work distinguishes, snow that reaches the ground and snow that sublimates before it. Radars at the ground are an established term of comparison for the spaceborne ones, and the CloudSat reflectivities were found to agree with those measured by ground-based and airborne cloud radars to within the calibration uncertainty of the reference instruments (Protat et al., 2009). In Antarctica, ground-based MRR profiles have already been compared with the satellite retrievals by Lemonnier et al. (2019), who evaluated the CloudSat snowfall profiles at two East Antarctic stations. The present work extends that comparison downward, below their lowest comparison heights to the ground.

https://doi.org/10.5194/egusphere-2026-6639
Preprint. Discussion started: 30 October 2026
© Author(s) 2026. CC BY 4.0 License.

The depth of the cluttered layer differs between the two missions, being roughly twice as deep for CloudSat (∼1000 m) as for EarthCARE (∼500 m). Since the sublimation occurs within this layer, the same falling snow translates into different surface estimates depending on which of the two geometries observes it, by an amount that only measurements taken inside the layer can quantify.

Ground-based profiling radars provide this missing link between the processes at the surface and the satellite-scale products. The complexity and cost of installing and maintaining scanning weather radar for precipitation monitoring in polar conditions have kept the number of such deployments low (Alexander et al., 2023; Ferrone et al., 2023). In this respect the MRR occupies a favourable position. It is compact and operates unattended year-round with modest power and maintenance requirements. This has made it the most widespread profiling radar at Antarctic stations (Peters et al., 2002; Maahn and Kollias, 2012), deployed at sites spread around the continent and increasingly with the data openly available, as surveyed in Appendix A.

Paired with an optical disdrometer, which anchors the radar reflectivity to the particle size distribution measured at the ground, the MRR covers the vertical structure and the surface level with two instruments that run continuously through the polar night and require little maintenance. The pair also brackets the layer of interest from both sides: the radar reports whether hydrometeors are still falling at its lowest gate, and the disdrometer whether any of them reaches the ground, so that what happens in between can be observed rather than assumed.

In this work we use four years of paired MRR and disdrometer observations at MZS, with the radar specifically set up with a fine vertical resolution (35 m), so that its lowest reliable gate is at just 105 m a.g.l., well below the BZ of any spaceborne radar. The aim is threefold: (1) to classify every profile by whether its echoes reach the near-surface levels, and, through the disdrometer, whether the snow reaches the ground itself; (2) to characterise the meteorological regimes associated with each outcome, also in comparison with the ERA5 reanalysis (Hersbach et al., 2020), which offers continuous coverage and is increasingly used as a reference for Antarctic precipitation; and (3) to quantify the consequences of observing from progressively higher lowest gates.

These questions are part of the agenda that the Antarctica InSync science plan (Arndt et al., 2026), the coordinated international programme leading to the next International Polar Year, sets out for the coming years. Its atmospheric theme (Schmale et al., 2026) lists the characterisation of cloud and precipitation properties and the structure of the boundary layer among the gaps to be closed, asks for profiles reaching from the surface to the low-level clouds and built on the records already running, and points to the modelling of clouds and precipitation as what such observations should improve.

The paper is organised as follows. Section 2 describes the observations, the classification and the blind-zone simulation. Section 3.1 then characterises the four-year record, Sect. 3.2 the virga occurrence and the associated regimes, and Sect. 3.3 the different surface snowfall estimates. The coupling of virga and snow accumulation in the ERA5 reanalysis is treated in Sect. 3.4, while Sect. 3.5 simulates the view of the satellite radars affected by the blind zone, for both the virga occurrence and the snowfall estimates. The implications of the results are discussed in Sect. 4. Section 5 recaps and concludes. Appendix A surveys the MRR deployments in Antarctica, Appendix B details the ERA5 grid-point choice, and Appendices C and D report the radiosonde assessment and the Z_e–SR relations with the per-year accumulation tables, respectively.

https://doi.org/10.5194/egusphere-2026-6639
Preprint. Discussion started: 30 October 2026
© Author(s) 2026. CC BY 4.0 License.

2 Data and methods

2.1 Ground-based observations at Mario Zucchelli Station

The core instrument of this study is the METEK Micro Rain Radar 2 (MRR-2) operated at the Italian Mario Zucchelli Station (74.694° S, 164.115° E) within the Antarctic Precipitation Properties (APP) project of the Italian National Antarctic Research Program (PNRA): a vertically pointing, frequency-modulated continuous-wave (FMCW) Doppler radar at 24 GHz (K band) (Peters et al., 2002), configured with 35 m vertical resolution over 31 range gates, i.e. up to ∼1085 m above ground level, similarly to the configuration adopted for GPM pre-launch campaigns (Adirosi et al., 2016, 2020), while the other Antarctic MRR deployments mentioned in Sect. 1 are commonly operated with 100 m gates covering heights between 300–3000 m. The fine configuration gives up the 1050–3000 m layer in exchange for a detailed sampling of the lowest kilometre, where the processes of interest of this study take place. The raw MRR spectra made available every minute are reprocessed with the procedure of Maahn and Kollias (2012) (ImProToo), which dealiases the Doppler spectra and aims to extend the nominal sensitivity to ~ -14 dBZ (a prerequisite for detecting the weak echoes typical of sublimating snowfall) and provides the equivalent reflectivity factor Z_e (dBZ) at 24 GHz, the mean Doppler velocity W ($\mathrm{m\,s^{-1}}$, instrument convention: positive downward, i.e. falling hydrometeors) and the spectral width σ_W ($\mathrm{m\,s^{-1}}$). Data used in the study are 5-min averages, obtained from the native 1-min profiles by averaging Z_e in linear units ($\mathrm{mm^6\,m^{-3}}$) before converting back to dBZ, and by arithmetic averaging for W and σ_W, in both cases requiring at least three valid minutes out of five. The two lowest gates and the uppermost one are discarded by the processing, the former because they fall in the near field of the antenna, the latter because it is too noisy (Maahn and Kollias, 2012). The usable column therefore consists of the 28 gates from ∼105 to ∼1050 m a.g.l. The third gate of the MRR-2, at ∼105 m, is the lowest reliable observation height. This is a factor of three lower than the lowest reliable gate of an MRR in the common configuration, which is typically ∼300 m. The record covers the four years 2020, 2021, 2023 and 2024 (2022 is excluded due to an instrument failure), with 7097, 8425, 8642 and 7198 hours of operation respectively.

An OTT Parsivel optical disdrometer (Löffler-Mang and Joss, 2000; Tokay et al., 2014), co-located with the radar, underpins the site-specific Z_e–SR relations used in Sect. 2.5, and its particle counts provide the surface term in the analysis of Sect. 3.5, where virga is examined at different heights. Its 1-min particle spectra are aggregated to the same 5-min resolution by summing the counts, again with the requirement of at least three valid minutes out of five, after discarding the minutes that collect fewer than ten particles in total, to remove spurious counts. The known limitations of this instrument for solid precipitation, in particular the ambiguous sizing of irregular snowflakes, are characterised by Battaglia et al. (2010) and are accounted for in the derivation of those relations (Bracci et al., 2022a).

The MRR-2 and the Parsivel are installed side by side on the roof of one of the prefabricated modules that house the station laboratories, as sketched in Fig. 1. The height coordinate used for MRR and Parsivel analyses is referenced to that deck. The deck stands at about 20 m above sea level, since the terrain at the station is about 15 m a.s.l. and the module and its supports raise the deck by roughly 5 m more. The curated datasets produced by the two instruments over the whole period are publicly available as separate archives for the radar profiles and for the disdrometer spectra (Roversi et al., 2026a, b), with the corresponding metadata records held by the Italian Antarctic Data Center (Baldini et al., 2025).

https://doi.org/10.5194/egusphere-2026-6639
Preprint. Discussion started: 30 October 2026
© Author(s) 2026. CC BY 4.0 License.

Ancillary near-surface observations are provided by the Italian Antarctic Meteo-Climatological Observatory (Climantartide, https://www.climantartide.it/). The observatory includes the Eneide automatic weather station (air temperature, pressure, relative humidity, wind speed and direction) (Grigioni et al., 2022a), and processed reports from Vaisala CL51 ceilometer (Grigioni et al., 2022b). The available CL51 observations contain reports at 5-min intervals of up to three layer heights (*Lh1–Lh3*) and the associated cloud amounts (*Lca1–Lca3*). We use the first archived height field, hereinafter ceilometer-reported height (CRH), together with the associated *Lca1* field reported in oktas, that is in eighths of the sky covered. The interpretation of CRH requires some consideration about signal attenuation by fog or precipitation. Native CL51 messages can report vertical visibility when such attenuation prevents cloud-base detection (Vaisala Oyj, 2025). Vertical visibility is an extinction-based viewing distance and does not locate a cloud boundary. The Vaisala Sky Condition algorithm can also incorporate vertical-visibility detections when estimating layer heights (Vaisala Oyj, 2024). However, the metadata of CL51 archive do not clarify whether or how these detections are represented in *Lh1*. In the absence of the original backscatter profiles and detection-status flags, a cloud-base interpretation cannot be established for every archived height. CRH is therefore retained as a descriptive observational variable and is not used to directly validate ERA5 cloud-base height. Ceilometers are a standard component of Antarctic observatories, with long records available for instance at Neumayer (Schmithüsen, 2022) and at Scott Base, where CL51 observations have also been used to evaluate the cloud representation of the reanalyses (McDonald et al., 2025). CRH and *Lca1* observations are used at hourly resolution to characterise the meteorological environment of the radar profiles. The weather station data are distributed as hourly values, while the ceilometer reports every 5 min and is aggregated to hourly resolution by the median of the layer heights detected within each hour. The same observatory performs the operational radiosoundings at 00 and 12 UTC, launched during the summer campaigns only, that are used in Appendix C to assess the ERA5 vertical structure.

2.2 ERA5 reanalysis

Besides the ground-based observations, we consider the ECMWF ERA5 reanalysis (Hersbach et al., 2020) at hourly resolution. The model provides a complete set of surface and pressure-level fields on a uniform grid with 0.25° lat/lon horizontal resolution. From the surface fields we use the snowfall flux (*sf*), which the model provides in m of water equivalent accumulated over the hour and which we report in mm w.e. throughout, the 2-m temperature (*t2m*, K) and dew point (*d2m*, K), needed to compute the relative humidity (with the Magnus formula with the coefficients of Alduchov and Eskridge, 1996), the 10-m wind components (*u10* and *v10*, $\mathrm{m\,s^{-1}}$), the cloud-base height (*cbh*, m) and the boundary-layer height (*blh*, m), the latter used in the grid-point assessment of Appendix B. From the pressure-level fields we use relative humidity (*r*, %), wind (*u* and *v*, $\mathrm{m\,s^{-1}}$) and geopotential (*z*, $\mathrm{m^2\,s^{-2}}$) on eleven levels between 1000 and 500 hPa, densified to 25-hPa spacing in the boundary layer, and the specific snow water content (*cswc*) on the same levels, which the model provides in $\mathrm{kg\,kg^{-1}}$ and which we report in $\mathrm{g\,kg^{-1}}$ throughout. Vertically resolved ERA5 snow water content is used in a similar way by Scarsi et al. (2025) to study the impact that ground clutter will have on WIVERN retrievals over different terrains.

All fields are extracted from the single cell that contains the station, centred at 74.75° S, 164.0° E, 7.1 km from MZS. Its physical setting is not a faithful copy of the station's, because MZS sits on a steep land–sea transition that the ERA5 model

https://doi.org/10.5194/egusphere-2026-6639
Preprint. Discussion started: 30 October 2026
© Author(s) 2026. CC BY 4.0 License.

resolution cannot follow: the ERA5 cell is coastal-mixed, with a land fraction of 0.55, and its model orography is 108 m, about 88 m above the real instrument elevation of 20 m.

Two consequences of this choice were assessed before using the reanalysis, and are reported in full in Appendix B. The first is whether the cell containing MZS is the best available proxy for the station. Taking the Eneide weather station as an independent arbiter, the chosen grid point reproduces the observed surface fields better than either the average of the four grid points surrounding the station or a bilinear interpolation to its location, because any spatial averaging blends in the colder and more elevated inland cells to the north. The wind direction is the one exception, being reproduced poorly by all three estimators alike, which points to an unresolved small-scale diurnal veering of the katabatic flow rather than to the grid-point choice, and is the reason why the ERA5 wind is discussed here in terms of speed rather than direction. The second aspect is how much the results depend on the selected pixel, tested by repeating the analysis over the 3×3 neighbourhood around the station. The quantities that carry the conclusions of this paper vary by less than 4 % across the nine cells, and every cell reproduces the ERA5 behaviour described in Sect. 3.2.2.

2.3 Spaceborne radar reference framework

Spaceborne cloud radars enter this study as a reference observation geometry rather than as a data source. The W-band Cloud Profiling Radars of CloudSat and EarthCARE cannot exploit their lowest range gates for atmospheric observations because of surface clutter, so each of them is bounded from below by its lowest reliable gate. We take the nominal height of that gate as the lowest observable height (LOH) of the system. The sublimation we want to measure acts over the layer below it. On this axis a surface instrument such as the disdrometer has LOH $= 0$, and systems with different range resolutions become comparable.

For the MRR-2 described above the LOH is 105 m a.g.l. One further height, 315 m, is the LOH of an MRR in the common 100-m configuration (lowest reliable gate at $\sim$300 m), so that the results at that height indicate what the other Antarctic MRR deployments can observe. The heights used in the following are summarised in Fig. 1.

For EarthCARE the CPR receiver response was designed to keep the surface clutter below the detection threshold above about 500 m (Lamer et al., 2020), and the height of 490 m used in the following is taken as the EarthCARE-like LOH. For CloudSat the clutter-affected layer over land is deeper. The CloudSat CPR 2B-GEOPROF product has a final vertical resolution of 240 m, and the first bin always free from ground clutter is the sixth, with a nominal height level of $\sim$1200 m (Maahn et al., 2014; Palerme et al., 2019). The CloudSat–ground comparison of Bracci et al. (2023) at MZS could use bins centred at 720 and 960 m a.s.l., after filtering with the C1 cloud mask scheme of Hagihara et al. (2010) and the signal-to-noise significance levels of Marchand et al. (2008). The native MRR gates closest to those two levels, at 700 and 945 m a.g.l. (i.e. 720 and 965 m a.s.l., given the $\sim$20 m station elevation), are therefore added as CloudSat-like LOHs, so that the two satellite records, which do not overlap in time, can be referred to the same ground-based framework. Each satellite-like LOH is simulated at the nominal height of the corresponding native MRR gate, thus retaining its 35-m sampling volume rather than reproducing the original CPR range resolution. The direct validation of EarthCARE level-2 products (Sato et al., 2025; Sato and Okamoto, 2025; Okamoto et al., 2025) against the MZS observations is the subject of a companion study.

https://doi.org/10.5194/egusphere-2026-6639
Preprint. Discussion started: 30 October 2026
© Author(s) 2026. CC BY 4.0 License.

2.4 Virga classification

Each 5-min MRR-2 profile is classified from the vertical distribution of its radar echoes, using the 105-m gate (the MRR LOH) as the lowest level of interest. Radar reflectivity at 24 GHz is taken directly from ImProToo, with only a cautionary threshold of -20 dBZ, which never filtered any of the 5-min profiles in the four-year record (the dataset minimum is -14.9 dBZ).

An MRR profile is classified as follows:

- *precipitation*, when the lowest gate and the two gates immediately above it all contain echoes. This three-gate vertical continuity requirement suppresses isolated near-surface clutter spikes.
- *virga*, when echoes are absent at the lowest gate but present aloft in at least two adjacent gates, or in either of the two uppermost gates, which indicates a column extending above the measurement range.
- *noisy*, when neither condition is met, i.e. for isolated returns with no vertical continuity.
- *no signal*, when the profile contains no echo at all.

No separate class is introduced for clouds that do not precipitate, because the MRR carries no information that would allow such samples to be identified. Any echo above the detection floor is already falling at a speed typical of snow, and that speed does not decrease towards the weakest echoes,[1] so no velocity criterion can isolate suspended particles. The no-signal label should accordingly be read as the absence of hydrometeors above the radar sensitivity, not as the absence of cloud. The ceilometer reporting conditions associated with these profiles are examined in Sect. 3.2.2.

The two- and three-gate continuity requirements were not set a priori, but follow from the vertical structure of the echoes in this record. Considering the profiles that contain signal, 84 % have a vertically contiguous echo, and where an internal gap is present it is usually narrow, with a median total width of 70 m (two gates) and 41 % of the cases confined to a single gate. Isolated returns are instead rare, as only 1.9 % of the signal-bearing profiles have a single gate above threshold. Requiring two adjacent gates aloft therefore rejects the isolated returns without discarding physically continuous columns, and the three-gate requirement at the base extends the same protection to the levels where clutter contamination is most likely. A continuity criterion of the same order, two to three levels, was adopted in the MRR virga detection algorithm developed for Ny-Ålesund (Saini et al., 2026a), which additionally exploits the Doppler velocity and height-dependent percentile thresholds.

A separate source of near-surface echoes at a katabatic site is blowing snow, which the continuity criteria alone cannot distinguish from precipitation reaching the ground. Its effect on the classification is one-sided, because lifted particles can only add signal at the lowest gates, so that a sublimating column may occasionally appear continuous and be counted as precipitation. The virga occurrences reported here are therefore conservative in this respect as well. A systematic discrimination is possible, either from the ceilometer backscatter, for which dedicated detection algorithms have been developed and applied

[1] Grouping the samples by reflectivity, the median Doppler velocity of the weakest bin (-15 to -10 dBZ) is 0.88 m s^{-1}, indistinguishable from that of the strongest returns. That value is a median and not a detection limit, as the dealiasing of Maahn and Kollias (2012) resolves the low and negative velocities as well.

https://doi.org/10.5194/egusphere-2026-6639
Preprint. Discussion started: 30 October 2026
© Author(s) 2026. CC BY 4.0 License.

at East Antarctic stations (Gossart et al., 2017), or by combining profiling and surface instruments as at Princess Elisabeth (Gorodetskaya et al., 2015), and is left outside the scope of this work.

When the classification is paired with hourly datasets (Eneide, CL51, ERA5), the twelve 5-min labels of each hour are aggregated by majority vote restricted to the signal-bearing classes, with ties resolved in the order: precipitation, virga, noisy. Instrument-off periods are identified from the time axis of the raw data files and excluded from all occurrence statistics.

2.5 Snowfall-rate estimation

Reflectivity at the LOH is converted to snowfall rate through the inversion of power-law Z_e–SR relations of the form $Z_\mathrm{e} = a\,\mathrm{SR}^{\,b}$, that is

$$\mathrm{SR} = \left(\frac{Z_\mathrm{e}}{a}\right)^{1/b}, \tag{1}$$

with Z_e in linear units ($\mathrm{mm^6\,m^{-3}}$) and SR in $\mathrm{mm\,h^{-1}}$ of snow water equivalent (SWE). The conversion is applied to each 5-min sample and the accumulation is the sum over the samples, so that the non-linearity of the relation acts on the individual reflectivities rather than on their average. Three relations, all calibrated at MZS, are used in parallel: the habit-dependent pair from combined MRR–Parsivel observations for aggregate-dominated and pristine-crystal conditions (Bracci et al., 2022a), and the long-term relation of Scarchilli et al. (2020). No attempt is made to select a best relation, and their spread is treated as the microphysical uncertainty of the ground-based estimate. That this uncertainty is dominated by the particle habit is not a peculiarity of this site. At Dome C, eight years of direct imaging of the falling crystals identify ten representative habits whose size distributions imply appreciably different reflectivities (Del Guasta et al., 2024). Spaceborne retrievals are also dominated by the same type of uncertainty, though synergistic approaches reduce it (Okamoto et al., 2010; Sato and Okamoto, 2011, 2023). The adopted coefficients and their ranges are listed in Table D1. For each relation, the uncertainty of the fitted parameters is propagated by Monte Carlo sampling, and the 5–95th percentile range of the resulting accumulations is reported alongside the central estimate.

Snowfall accumulation from ERA5 is computed from the snowfall flux variable (*sf*). To evaluate the near-surface description provided by the MRR, the hourly model series is then matched in time with the radar classification and screened between the different MRR classes, eventually retaining only the hours classified as precipitation. The difference between the raw and the screened accumulation is the model snowfall deposited when the radar sees no precipitation reaching the ground. Hours without radar measurements are left out of this process, but they carry an appreciable share of the accumulation only in 2020 and 2024, the years with the longest gaps in radar measurements.

2.6 Simulation of satellite lowest observable height

2.6.1 Virga occurrence below the satellite LOH

The MRR-based classification in precipitation, virga or noisy profiles is repeated with each usable range gate taken in turn as the lowest reliable one, i.e. the simulated LOH rises gate by gate, in steps of the native 35-m MRR resolution, from 105

https://doi.org/10.5194/egusphere-2026-6639
Preprint. Discussion started: 30 October 2026
© Author(s) 2026. CC BY 4.0 License.

up to ∼980 m (the last gate at which the three-gate continuity requirement stays within the measured profile). This simulates the view of an instrument that cannot see below a given height (in particular the CPR-like geometries defined above) while keeping everything else identical. Profiles whose echo terminates between the true LOH and the simulated one migrate from being classified as virga to precipitation. The surface snowfall estimated at the simulated LOH also incorporates the snow that sublimates below it.

The sweep is also extended one step in the opposite direction, below the radar, by taking the disdrometer as the observing system at LOH $= 0$. A profile is then classified as precipitation when the Parsivel records particles at the ground and the column above it satisfies the same three-gate condition at 105 m, and as virga either when the radar column is virga, or when the radar sees precipitation at 105 m while the disdrometer records no particle. Requiring the radar signal as well protects the ground term against blowing snow, whose particles reach the disdrometer without originating from the precipitation aloft. The same ground check is applied to the accumulation, by retaining only the hours of the already screened set in which the disdrometer records particles. Since the Parsivel record is limited to the summer months in 2021 (Table 1), both occurrence and accumulation estimates at LOH $= 0$ are computed on the other three years only.

2.6.2 Snowfall sublimation lost below the LOH

Finally, to estimate how much of the snowfall lost to sublimation goes unobserved because it happens below each simulated LOH, we adapt the sublimation ratio *SubR* of Bracci et al. (2022b) to accumulations and express it in per cent:

$$\mathrm{SubR}_i = \frac{\mathrm{SWE}_i - \mathrm{SWE}_{105\,\mathrm{m}}}{\mathrm{SWE}_{105\,\mathrm{m}}} \times 100, \tag{2}$$

where SWE_i is the snowfall accumulation estimated from the reflectivity at the simulated LOH i, and $\mathrm{SWE}_{105\,\mathrm{m}}$ the one estimated at the MRR-2 lowest reliable gate (105 m). Normalised by the reference gate, SubR_i is the overestimation that a surface estimate taken at the LOH i carries with respect to the one at 105 m.

3 Results

The results are presented in three steps. We first describe the four-year record and the radar profiles through frequency by altitude diagrams and seasonal quantiles, which show precipitation at MZS to be episodic, present in all seasons, and to change character in the lowest few hundred metres of the profile. We then apply the classification described in Sect. 2.4, which assigns to virga more than 1 column in 3 among those containing hydrometeors, and we show that the classes correspond to distinct meteorological regimes in observations and reanalysis fields that carry no information from the radar. We finally convert the reflectivities at the LOH into surface snowfall estimates, use the classification to constrain the accumulation of the reanalysis, and quantify the sensitivity of the yearly accumulation to a varying LOH, simulating the effects of the spaceborne radars' BZ.

https://doi.org/10.5194/egusphere-2026-6639
Preprint. Discussion started: 30 October 2026
© Author(s) 2026. CC BY 4.0 License.

Table 1. Summary of the four-year MRR record and of its classification. Hourly classes are obtained by majority vote of the twelve 5-min labels of each hour, restricted to the classes that carry a signal. The 5-min class occurrences are given as percentages of all valid profiles, no-signal included, and in brackets as percentages of the signal-bearing profiles only. The last column gives the hours measured by the co-located Parsivel disdrometer, counted as for the MRR. The 2021 coverage is limited to January, February, November and December, so that year is excluded from all the Parsivel-based statistics.

Year	MRR hours (% of year)	Valid 5-min profiles	Hours with echo (% of measured)	Hourly classes (h)			5-min occurrence, % of valid (of signal)		Parsivel hours (% of year)
				Precip.	Virga	Noisy	Precip.	Virga	
2020	7097 (80.8 %)	85 136	1194 (16.8 %)	600	568	26	7.2 (59.2)	4.6 (37.4)	7102 (80.9 %)
2021	8425 (96.2 %)	100 991	1573 (18.7 %)	739	806	28	7.5 (55.9)	5.5 (41.2)	2567 (29.3 %)
2023	8642 (98.7 %)	103 680	1219 (14.1 %)	697	497	25	6.8 (65.5)	3.3 (32.2)	8735 (99.7 %)
2024	7198 (81.9 %)	86 273	1145 (15.9 %)	534	591	20	6.7 (55.6)	5.1 (42.4)	8719 (99.3 %)
Total	31 362 (89.4 %)	376 080	5131 (16.4 %)	2570	2462	99	7.1 (58.9)	4.6 (38.4)	27 123 (77.3 %)

3.1 Four years of precipitation profiles at MZS

The record analysed here covers four full years of MRR operation at MZS, namely: 2020, 2021, 2023 and 2024, with 2022 excluded due to an instrument failure. Over these four years the radar measured for a total of 31 362 hours, corresponding to between 81 % (2020, worst year) and 99 % (2023, best year) of each calendar year (Table 1). Hydrometeor echoes were detected in 5131 hours, i.e. 16.4 % of the measured time, with a moderate inter-annual spread (14.1–18.7 %) and no year standing out as anomalous. Since MZS is a summer station, and is unattended during the polar night, hardware problems requiring hands-on maintenance can only be resolved with the arrival of the station technical staff in November (Fig. 2, bottom panel). The gaps therefore tend to accumulate towards the end of the winter, and September and October are the least represented months of the record (69 and 75 % of the hours available over the four years), followed by February (80 %), which is affected by an outage in 2024. We verified that this uneven coverage does not appreciably bias the statistics presented below: imposing the observed gap patterns of the incomplete years onto the nearly complete ones (2021, 2023) changes the annual echo-hour fraction by at most 2.2 percentage points, less than its inter-annual spread, and the echo fractions of the under-sampled months lie within the range spanned by the other months.

Figure 2 shows the full record as one panel per year. Precipitation at MZS is episodic. Echoes are organised in discrete events, typically lasting from several hours to a few days, separated by long dry intervals, and occurring in all seasons and in all years without any echo-free month (when measured). The curtain already anticipates what will emerge from the analysis of Sect. 3.2. Many echo columns span the whole observed range down to the lowest gates, while a substantial number of them fade before reaching the bottom of the profile. This is a first qualitative indication of low-level depletion of the falling snow.

The aggregated statistics of the three radar variables are summarised in the contoured frequency by altitude diagram (CFAD; Yuter and Houze, 1995) of Fig. 3. The Z_e distribution is narrower in the upper part of the profile, with a well-defined mode around -5 dBZ near 1 km, and broadens toward the ground, where the distribution spreads over more than 25 dB while the median decreases slightly. This behaviour is consistent with the coexistence of the two populations examined in Sect. 3.2:

https://doi.org/10.5194/egusphere-2026-6639
Preprint. Discussion started: 30 October 2026
© Author(s) 2026. CC BY 4.0 License.

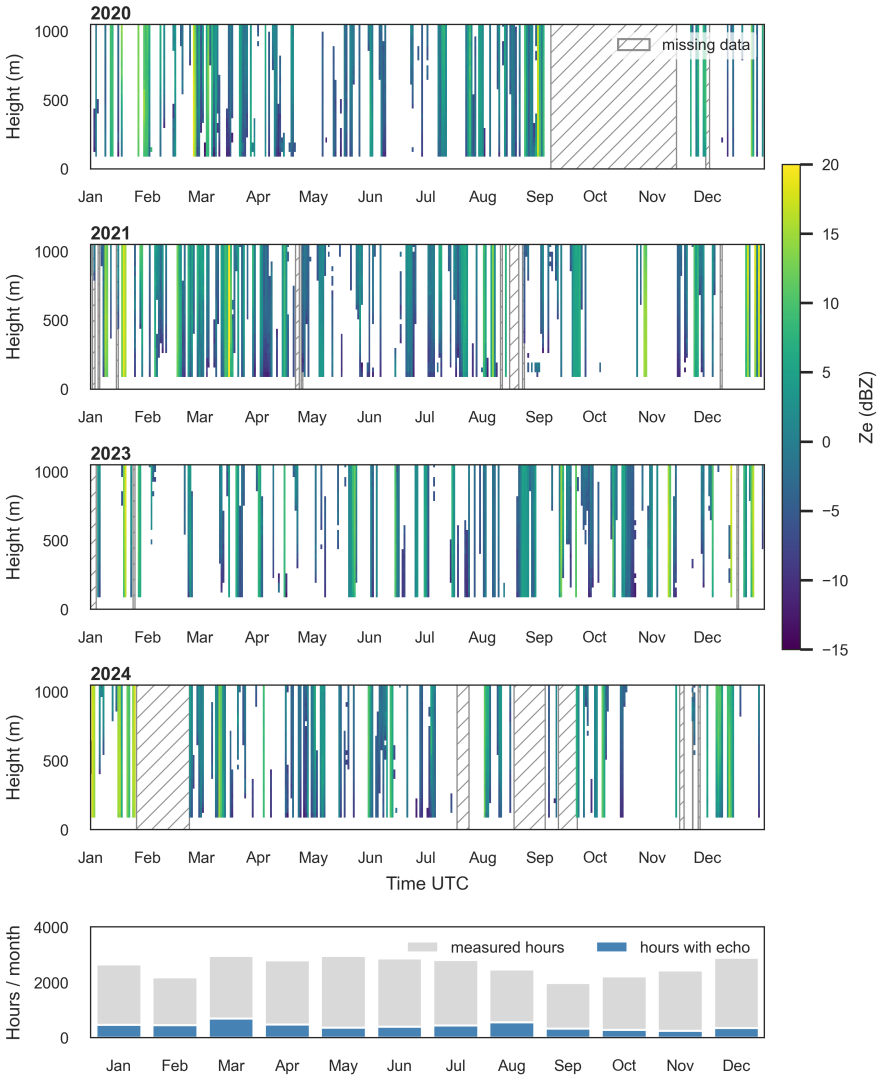

Figure 2. Daily Z_e curtain plot of the four-year MRR record at MZS, one panel per year (colour: daily linear-mean Z_e of echo samples; grey: instrument off; 2022 is excluded). Bottom: month-of-year distribution of measured hours and hours with radar echo, pooled over the four years.

columns in which particles keep growing on their way down, and echoes progressively weakening towards the ground. The Doppler velocity is remarkably uniform: the median W lies between $+0.7$ and $+0.9$ m s^{-1} (positive downward) at all heights, with the 5–95th percentile band confined within roughly -0.2 and $+1.5$ m s^{-1}, as expected for dry snowfall with limited riming. The spectral width has a mode near 0.2 m s^{-1} throughout the column, and its 95th percentile broadens below ∼300 m. This broadening is not accompanied by a shift of the median Doppler velocity, which constrains its interpretation. Riming

https://doi.org/10.5194/egusphere-2026-6639
Preprint. Discussion started: 30 October 2026
© Author(s) 2026. CC BY 4.0 License.

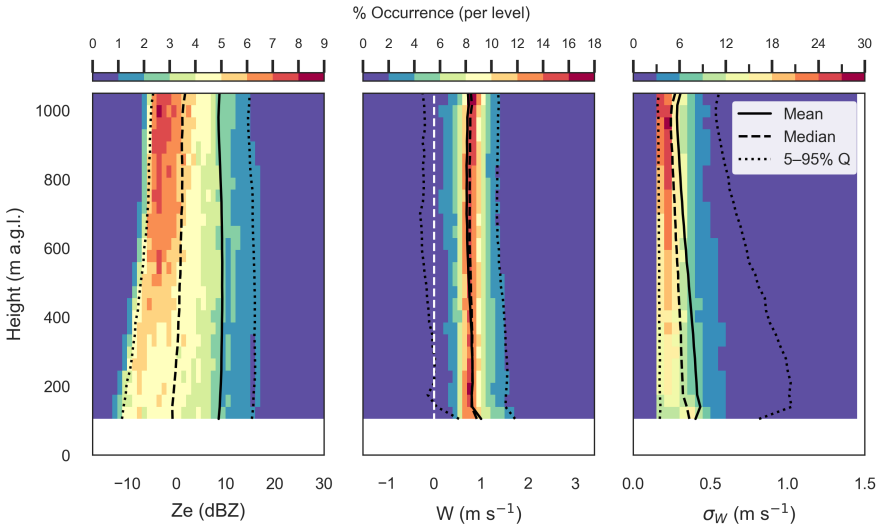

Figure 3. CFAD of Z_e, W and σ_W (occurrence normalised per height level; discrete colour levels) with mean, median and 5–95th percentile profiles, four-year record. Z_e statistics computed in linear units; W follows the instrument convention (positive = downward, falling snow).

increases the particle mass rapidly and with it the terminal velocity, so it shifts the Doppler peak rather than merely widening it (Kneifel and Moisseev, 2020; Chellini et al., 2022). The same applies to melting, which the surface temperature rules out, since it reaches 0 °C in 0.5 % of the precipitation hours. The near-surface broadening therefore points to turbulence and wind shear, or more generally to an increased microphysical variability in the lowest layers, rather than to systematic particle growth. A residual contribution of ground clutter at the lowest gates cannot be excluded. The class-conditioned profiles of Sect. 3.2 help separate these contributions.

The seasonal overlay of Fig. 4 shows that summer (DJF) profiles are shifted toward higher reflectivities, with a median Z_e about 5 dB higher than in winter (JJA), and exhibit a slightly larger median W, while the shape of the profiles is preserved across seasons. A similar seasonal contrast in Doppler velocity, higher in summer and lower in winter, was also reported for the 7-year MRR record at Dumont d'Urville by Wiener et al. (2024), suggesting that this is a recurrent feature of coastal Antarctic snowfall rather than a peculiarity of the Terra Nova Bay site. Year-to-year differences of the median profiles are small compared with the seasonal contrast, and no monotonic multi-year trend is apparent in the four-year record.

3.2 MRR-based classification of precipitation, virga and no-signal profiles

3.2.1 Virga occurrence and MRR radar signatures

Applying the classification of Sect. 2.4 to the four-year record, 58.9 % of the signal-bearing 5-min profiles are classified as *precipitation*, 38.4 % as *virga* and 2.7 % as *noisy*. At MZS, more than 1 column in 3 in which the radar detects hydrometeors does not produce any echo at the lowest reliable gate (105 m). The virga share is a persistent feature of all four years, although

https://doi.org/10.5194/egusphere-2026-6639
Preprint. Discussion started: 30 October 2026
© Author(s) 2026. CC BY 4.0 License.

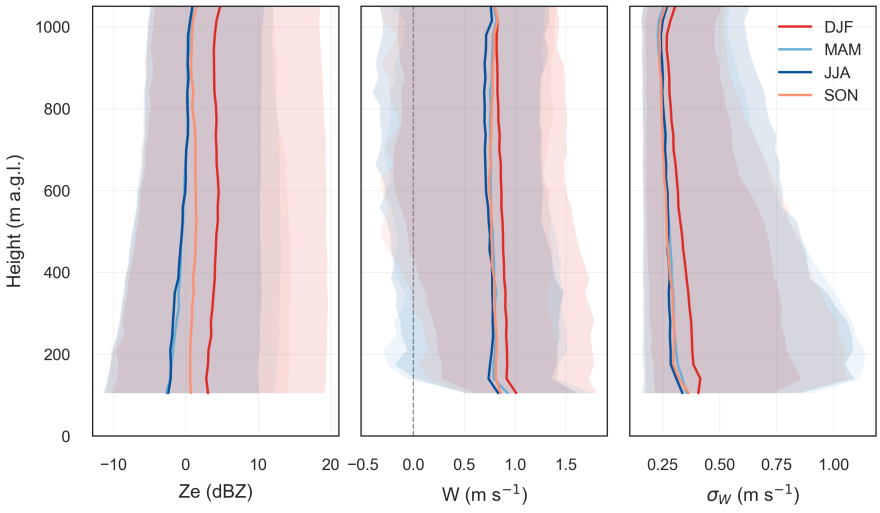

Figure 4. Seasonal median profiles (DJF/MAM/JJA/SON) of Z_e, W and σ_W with 5–95th percentile bands (shading).

with substantial inter-annual variability (from 33 % in 2023 to 43 % in 2024 of the hydrometeor-bearing samples, noisy ones excluded). The gap simulation of Sect. 3.1, repeated on the class fractions, changes them by at most 3.2 percentage points, again well within the inter-annual spread.

The three classes differ markedly in their vertical structure (Fig. 5). Precipitating columns have the strongest echoes among the classes at all heights and are nearly uniform along the vertical. Their median reflectivity decreases downward by less than 4 dB, from a ∼5 dBZ plateau above 700 m to 1.5 dBZ at the lowest gate. Virga columns are 6–7 dB weaker at the same heights and fade toward the ground on both counts: the median falls by about 8 dB over the same layer, and progressively fewer samples reach the lower gates (none at 105 m, by construction). What changes downward is therefore the balance between the two populations (Fig. 5, first two rows), precipitation growing from 61 % of the signal-bearing samples near 1 km to 98 % at the lowest gate, and not the intensity of the echoes themselves. The median Doppler velocity is nearly identical in the two classes (∼0.7–0.8 m s^{-1}), indicating similar particle populations aloft. The spectral width, in contrast, broadens toward the ground only in the precipitating columns. This is the class-conditioned view anticipated in Sect. 3.1, and it attributes the near-surface σ_W broadening of the aggregated CFAD to the columns that do reach the ground. The noisy class is dominated by isolated near-surface returns. The few samples it contributes higher up, however, follow the virga structure (Fig. 5, bottom row: a weak median reflectivity fading downward, within 1–2 dB of the virga medians) rather than the precipitation one, suggesting that part of these profiles are fragments of virga-like echoes rejected by the vertical-continuity test.

3.2.2 Meteorological regimes associated with the classes of MRR profiles

The classification is built on the radar profiles alone (Sect. 2.4), so any separation it produces in quantities that the radar does not measure provides an independent check on it, and also associates the occurrence of the classes with specific meteorological

https://doi.org/10.5194/egusphere-2026-6639
Preprint. Discussion started: 30 October 2026
© Author(s) 2026. CC BY 4.0 License.

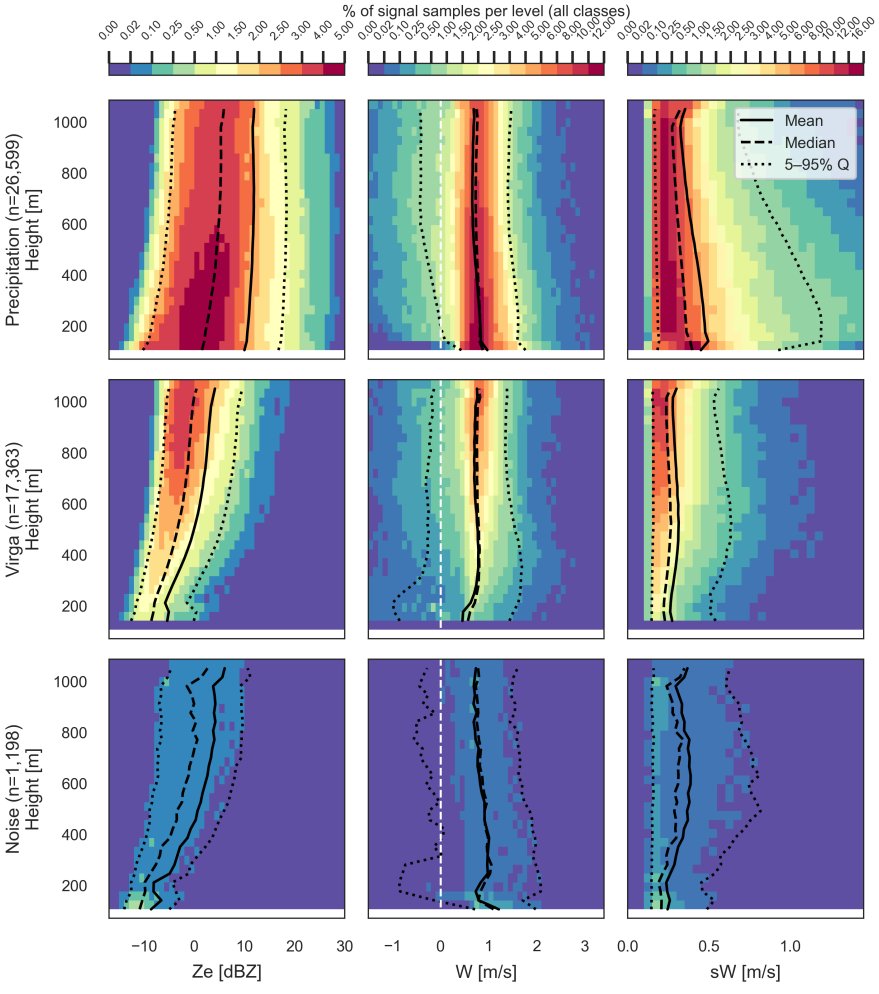

Figure 5. CFADs of Z_e, W and σ_W conditioned on the MRR classification (rows: precipitation, virga, noisy; 5-min samples, four-year record), with mean, median and 5–95th percentile overlays. The occurrence is normalised per height level by the total number of signal-bearing samples of all classes, so that the three rows of each column decompose the aggregated CFAD of Fig. 3 and the colour weight reflects the relative frequency of each class; colour levels are shared within each column.

conditions. The radar signatures of Fig. 5 already show that the three classes correspond to distinct phenomena. They also correspond to distinct meteorological regimes that can be seen in observations carrying no MRR information (Fig. 6). At the surface, the Eneide relative humidity decreases monotonically from *precipitation* (median 82 %) to *virga* (61 %) to *no-signal* hours (46 %). CRH increases in the same class order, with hourly medians of approximately 0.5, 1.1 and 2.5 km, respectively. This ordering describes differences in the ceilometer output and cannot be attributed uniquely to differences in cloud-base height, because obscuration can affect the reported values as described in Sect. 2.1. The lower surface humidity during virga is

https://doi.org/10.5194/egusphere-2026-6639
Preprint. Discussion started: 30 October 2026
© Author(s) 2026. CC BY 4.0 License.

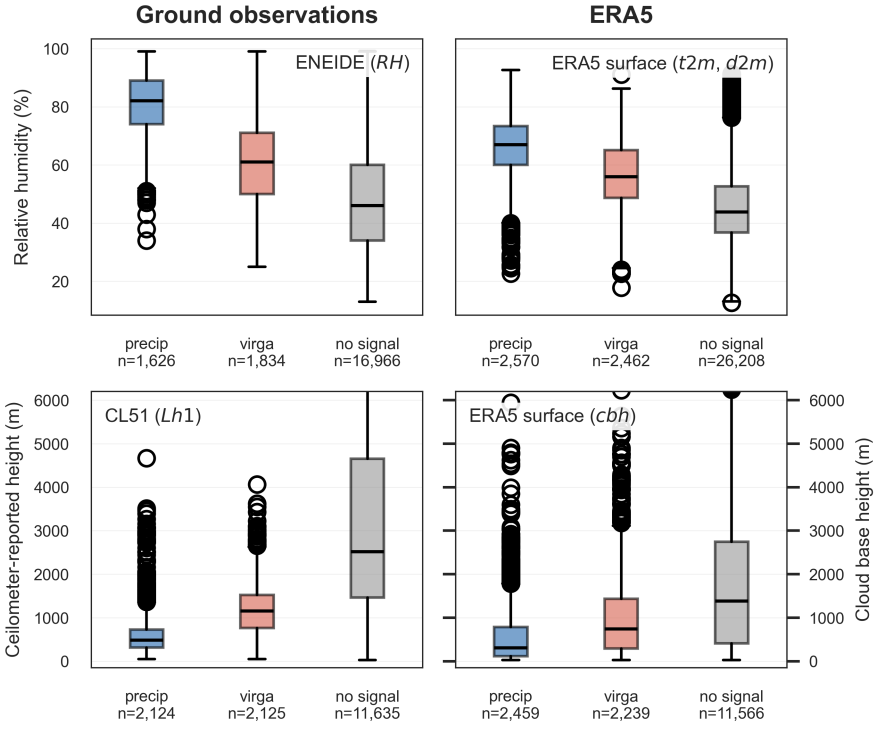

Figure 6. Meteorological and ceilometer diagnostics by MRR class at hourly resolution. The upper panels show surface relative humidity from Eneide (left) and ERA5 (right), with ERA5 relative humidity calculated from *t2m* and *d2m*. The lower panels show CL51 ceilometer-reported height (CRH, left) and ERA5 cloud-base height (*cbh*, right), shown side by side for description only. No pressure-level field is used here. Shared y-axis within each row. Height outliers above 6.2 km (up to ∼13 km) are not shown.

consistent with conditions favouring the depletion of falling snow. Precipitation occurs preferentially with south-westerly flow (Fig. 7), whereas virga hours are dominated by the west-north-westerly sector associated with the katabatic drainage, with the highest wind speeds, that also characterises hours without radar signal. ERA5 reproduces the same qualitative separation for humidity and cloud base height, although with weaker contrasts (RH medians of 67, 56 and 44 %), and a markedly less realistic surface wind. Speeds are strongly underestimated and the directional distribution is concentrated in fewer sectors, blurring the distinction between the precipitation and virga regimes (note the different radial scales in Fig. 7).

The reanalysis is more informative above the surface, where its pressure-level profiles distinguish the three classes (Fig. 8). During virga hours the reanalysis shows a moist column aloft (median RH above 85 % between roughly 1.5 and 5 km) overlying a pronounced dry layer in the lowest few hundred metres, with a minimum around 950 hPa (∼300 m). During precipitation the column remains moist down to the surface, and during no-signal hours it is dry below 700 hPa. The virga RH profile is indistinguishable from the precipitation profile above ∼800 hPa (medians within a few percentage points), whereas in the dry layer it departs from it by 15–25 percentage points and approaches the no-signal values. The separation in RH between

https://doi.org/10.5194/egusphere-2026-6639
Preprint. Discussion started: 30 October 2026
© Author(s) 2026. CC BY 4.0 License.

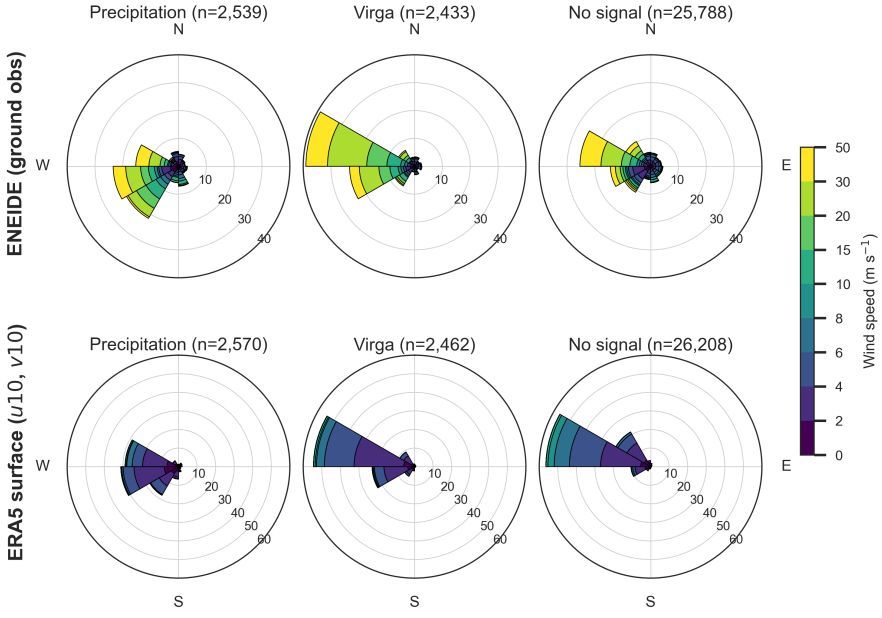

Figure 7. Wind roses by MRR class: Eneide observations (top) and the ERA5 surface wind (*u10* and *v10*, bottom). Speed bins are common to all panels. The radial (occurrence) scale is set per row for readability: note the different limits (40 % vs 60 %) when comparing rows.

the MRR classes is comparable to (or locally even larger than) the spread within each class, although the MRR classification uses no information from the reanalysis. Temperature differences between the classes are comparatively small (not shown), while the wind components separate the circulations. Near the surface all classes share the westerly katabatic outflow, but aloft the precipitation and virga hours exhibit an easterly zonal component, consistent with a synoptic origin of the flow, whereas no-signal hours remain westerly throughout the column. The model's own falling snow, however, does not follow the thermodynamic contrast (Fig. 8, right panel). The median snow-content profile of the virga hours crosses the dry layer nearly unchanged down to the lowest levels. The ERA5 thermodynamics thus captures the essential ingredient of the virga regime, the katabatic-driven dry layer below cloud base, but its prognostic snow largely survives it. *cswc* is still present at 975 hPa, the pressure level that lies at the model surface, in 68 % of the virga hours, against 88 % of the precipitation hours and 10 % of the no-signal hours (Fig. 9). The surface field behaves in the same way. Taking as precipitating the hours with a snowfall rate above 10^{-4} mm h^{-1}, ERA5 deposits snow at the ground in 90 % of the virga hours, against 96 % of the precipitation hours and 38 % of the no-signal hours. The implications of this behaviour for the model surface accumulation are quantified in Sect. 3.3. A local radiosonde assessment of the representativeness of the ERA5 vertical profiles during the summer months is reported in Appendix C.

The no-signal class accounts for most of the record. Its label describes the absence of MRR-detected hydrometeors rather than the actual absence of clouds (Sect. 2.4). Table 2 summarises the associated CL51 reporting conditions using the 5-min MRR classification and the available 5-min ceilometer reports. Among the matched no-signal profiles, 53.5 % have *Lca1* =

https://doi.org/10.5194/egusphere-2026-6639
Preprint. Discussion started: 30 October 2026
© Author(s) 2026. CC BY 4.0 License.

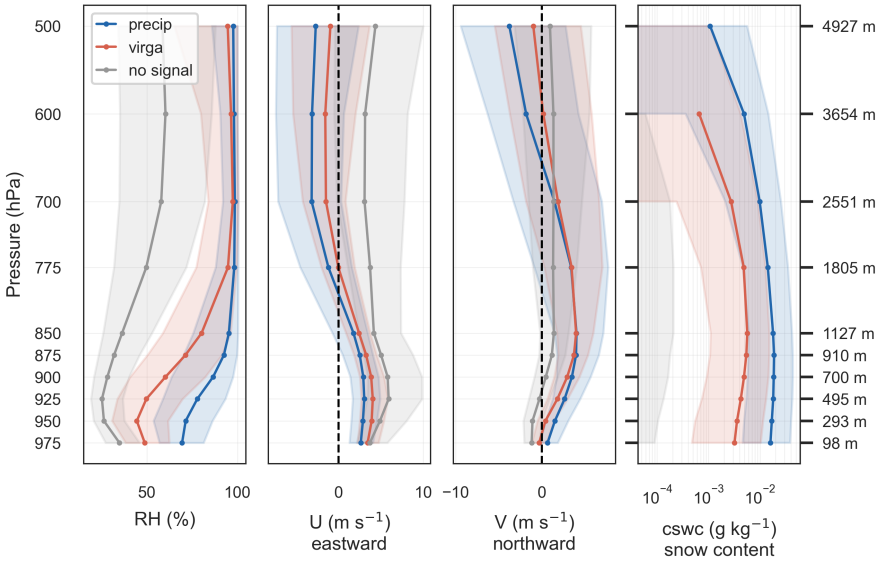

Figure 8. ERA5 pressure-level profiles by MRR class (shading: interquartile range): relative humidity, zonal (U) and meridional (V) wind components, and snow content (*cswc*, logarithmic axis). Median *cswc* values of zero (no snow in at least 50 % of the hours) are not drawn. Right axis: median geopotential height of the pressure levels. The profiles stop at 975 hPa, whose median height of 97 m is the model surface itself (orography 108 m). The 1000-hPa level lies below it in essentially all hours and is extrapolated, so it is not shown.

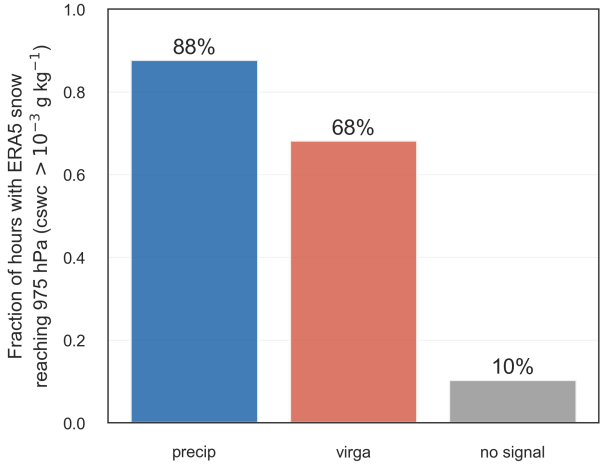

Figure 9. Fraction of hours in which ERA5 snow content is present at 975 hPa, the pressure level lying at the model surface (*cswc* $>$ 10^{-3} g kg^{-1}), by MRR class.

https://doi.org/10.5194/egusphere-2026-6639
Preprint. Discussion started: 30 October 2026
© Author(s) 2026. CC BY 4.0 License.

Table 2. CL51 reporting conditions for each MRR class, at the native 5-min resolution of both instruments. A time step is counted as zero okta when the ceilometer reports no cloud amount in the first layer, which is also when no height is reported. The remaining steps are split according to whether the ceilometer-reported height (CRH) falls below or above 1050 m, the top of the column sampled by the MRR. The last column gives the median CRH over the steps of the class that carry a reported height. The table covers the 324 836 valid MRR profiles (86.4 % of the record) for which a co-located ceilometer record exists.

MRR class	5-min steps	Zero okta		CRH $<$ 1050 m		CRH $\geq$ 1050 m		Median CRH
		n	%	n	%	n	%	(m)
Precipitation	22 270	314	1.4	19 658	88.3	2298	10.3	460
Virga	15 493	168	1.1	7784	50.2	7541	48.7	1030
Noisy	1007	25	2.5	629	62.5	353	35.1	785
No signal	286 066	153 093	53.5	27 301	9.5	105 672	36.9	2250

0, indicating zero reported cloud amount, 36.9 % have CRH at or above 1050 m, whereas 9.5 % have CRH below 1050 m. In the first group no height is reported either, so the absence of a CRH marks a clear sky rather than a gap in the ceilometer record. The last group comprises 27 301 steps over the four years and has a median CRH of 630 m. These categories describe the distribution of the ceilometer reports and do not unambiguously locate cloud bases relative to the MRR sampling range. In the precipitation class, 88.3 % of the matched reports have CRH below 1050 m, and the median CRH is 460 m (below the top MRR gate). For virga, 50.2 % have CRH below 1050 m and 48.7 % at or above that height.

3.3 Surface accumulation from the radar and from the reanalysis

The quantity that matters for the surface mass balance, and for most of the applications that motivate the measurement of Antarctic precipitation, is the snow that accumulates at the ground. In this section, the MRR reflectivities at the lowest reliable gate are converted into surface accumulations and compared with the surface snowfall from reanalysis.

Figure 10 compares, for each year, the surface accumulation estimated by the MRR at 105 m with the three MZS-calibrated Z_e–SR relations (coefficients in Table D1), the raw ERA5 surface snowfall and the ERA5 snowfall screened with the MRR classification, together with the decomposition of the discarded model snowfall introduced in Sect. 2.5. The two bands therefore separate what the reanalysis deposits during the virga hours from what it deposits when the radar records no signal or isolated echoes only, while the residual up to the raw curve is the snowfall falling during the instrument gaps of 2020 and 2024, the same gaps marked in Fig. 2.

The spread among the Z_e–SR relations dominates the uncertainty of the ground-based estimate. Over the four years the accumulation ranges from 213 mm SWE (Bracci Aggregates) to 425 mm (Scarchilli), reflecting the microphysical assumptions discussed in Sect. 2.5. ERA5 accumulates far more than any MRR-based estimate, namely 624 mm over the four years, i.e. between 1.5 and 3 times the ground-based range.

https://doi.org/10.5194/egusphere-2026-6639
Preprint. Discussion started: 30 October 2026
© Author(s) 2026. CC BY 4.0 License.

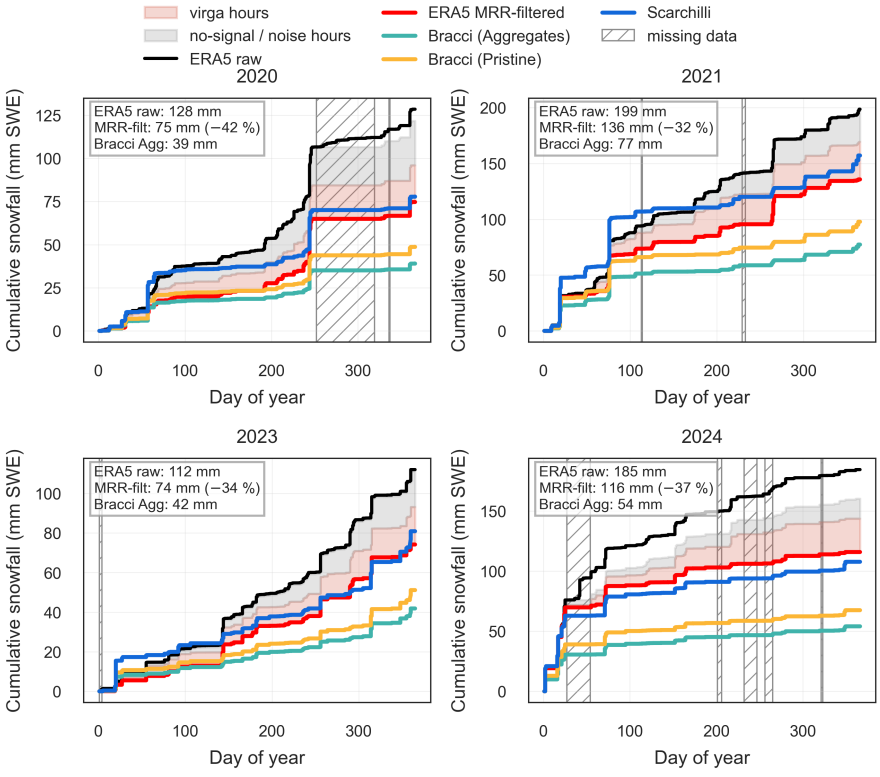

Figure 10. Cumulative surface snowfall per year: ERA5 raw (black), ERA5 filtered with the MRR classification keeping precipitation hours only (red line), and MRR-based Ze–SR estimates at 105 m. The gap between the precipitation-only filter and ERA5 raw is decomposed by MRR class into two stacked bands: the ERA5 accumulation falling during virga hours (pink) and during no-signal or noisy hours (grey). The residual up to ERA5 raw corresponds to MRR missing data, marked by the vertical grey fill patterns.

3.4 Constraining the ERA5 accumulation with the radar classification

The MRR classification can also be used to constrain the ERA5 accumulation directly (Fig. 10). Screening all hours of the reanalysis and keeping in the accumulation only the ones classified as *precipitation* removes 32–42 % of the raw ERA5 accumulation, depending on the year (400 mm w.e. in total, against 624 mm w.e.). A less strict choice, retaining the precipitation and the virga hours as well, would recover 102 mm over the four years, which is the size of the virga contribution (Fig. 10, virga band). The remaining 122 mm fall in the hours with no radar signal or with isolated echoes only (89 mm) and in the hours without radar data (33 mm). The decomposition of the ERA5 accumulation by MRR class (Fig. 11) indicates that the surplus in the reanalysis with respect to the ground estimates is structured in two components, one linked to the occurrence of precipitation and one to its intensity. About 36 % of the ERA5 snowfall mass (16.3 % in virga hours, 14.2 % with no radar signal or

https://doi.org/10.5194/egusphere-2026-6639
Preprint. Discussion started: 30 October 2026
© Author(s) 2026. CC BY 4.0 License.

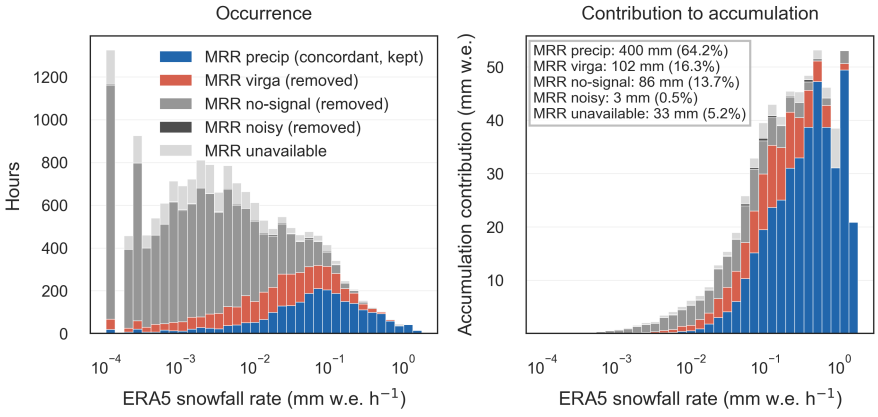

Figure 11. Distribution of ERA5 surface snowfall rates ($> 10^{-4}$ mm h^{-1}) by MRR class at 105 m (left: hours per log-spaced rate bin; right: contribution to the four-year accumulation). Light grey: hours with the MRR unavailable.

isolated echoes only, 5.2 % with the MRR unavailable) falls when the radar shows no precipitation reaching the ground. This is the occurrence component, the one that the class screening described above removes by construction.

The remaining 64 % of snowfall mass falls in concordant precipitation hours, yet the filtered ERA5 accumulation (400 mm) still lies at the upper end of the MRR-based range (213–425 mm). This is the intensity component. The agreement between the reanalysis and the ground-based estimates depends on the choice of the Z_e–SR relation, and appears to be strongly rate-dependent (Fig. 11, left). The median ERA5 snowfall rate is 0.0016 mm h^{-1} in the no-signal hours, about ten times larger in the virga hours (0.017 mm h^{-1}) and four times larger again in the precipitation hours (0.073 mm h^{-1}). The fraction of concordant hours grows monotonically with the ERA5 rate and exceeds 50 % only above ∼0.1 mm h^{-1}. The transition is however gradual, and the three classes coexist at the intermediate rates.

3.5 Blind-zone simulation

The *virga* occurrence of Sect. 3.2 and the accumulation of Sect. 3.3 can now be recomputed together, raising the LOH from the 105 m of this study to the higher values typical of the CPR on board EarthCARE and CloudSat. The answer defines the size of the BZ problem at this site.

The dependence of the estimates on the LOH (the CPR blind-zone simulation of Sect. 2.6) is summarised in Fig. 12 and Table 3. Raising the LOH from 105 to 490 m reclassifies part of the virga as precipitation. Followed profile by profile, 35 % of the columns that are virga at 105 m appear as precipitation at the EarthCARE-like LOH of 490 m, and 52 and 65 % at the CloudSat-like LOHs of 700 and 945 m. Over the columns that still carry an echo at or above the LOH, the virga share therefore decreases from 38.4 % at 105 m to 25.8 % at 490 m and 17.3 % at 700 m, and the apparent precipitation occurrence increases accordingly. Above ∼900 m both shares are increasingly set by the top of the measured profile, which leaves only a few gates above the LOH for the continuity checks, and the noisy share grows. The effect on the accumulation is systematic across all

https://doi.org/10.5194/egusphere-2026-6639
Preprint. Discussion started: 30 October 2026
© Author(s) 2026. CC BY 4.0 License.

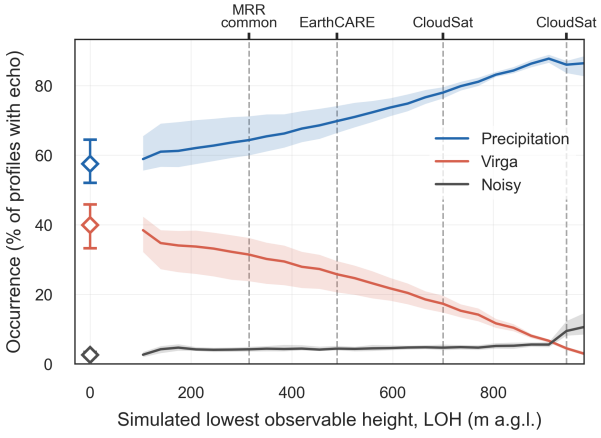

Figure 12. Occurrence of the MRR classes as a function of the simulated LOH, in m a.g.l., over the profiles with an echo at or above the LOH (lines: four-year percentages; bands: inter-annual range). The diamonds at LOH = 0 are the Parsivel-based ground points, computed on the years with Parsivel coverage (2020, 2023, 2024; bars: inter-annual range). Dashed lines mark the LOH of the most common configuration of MRR in Antarctica (315 m), the EarthCARE-like one (490 m) and the CloudSat-like ones (700, 945 m) defined in Sect. 2.3 and named on the top axis.

Table 3. Four-year (2020–2021, 2023–2024) SWE accumulation (mm) estimated from the MRR at increasing lowest observable heights (LOH; 315 m: common-configuration MRR; 490 m: EarthCARE-like; 700/945 m: CloudSat-like, cf. Sect. 2.3), for the three MZS-calibrated Z_e–SR relations, the aggregate (Aggr.) and pristine (Pris.) relations of Bracci et al. (2022a) and the one of Scarchilli et al. (2020), whose coefficients are listed in Table D1 (parentheses: 5–95 % Monte Carlo envelope; brackets: change relative to 105 m). The 0 m column holds the surface references: the ERA5 raw snowfall (*sf*, a surface flux by definition) and, for the Z_e–SR relations, the 105-m estimate retaining only the hours with hydrometeor counts at the co-located Parsivel. The asterisk marks that these cells are computed on the three years with disdrometer coverage (cf. Table 1), and that the change in brackets is relative to the 105-m accumulation over the same three years, which is 136, 168 and 268 mm for the three relations in the order of the rows. Per-year tables are given in Appendix D.

Relation	0 m (surface)	105 m	315 m	490 m	700 m	945 m
Bracci (Aggr.)	128 (113, 145)* [−6 %]	213 (189, 239)	256 (227, 286) [+20 %]	275 (243, 308) [+29 %]	285 (252, 321) [+34 %]	279 (245, 315) [+31 %]
Bracci (Pris.)	159 (139, 181)* [−6 %]	266 (234, 302)	321 (282, 364) [+21 %]	345 (303, 391) [+29 %]	357 (313, 405) [+34 %]	346 (302, 394) [+30 %]
Scarchilli	253 (241, 265)* [−6 %]	425 (406, 446)	514 (491, 539) [+21 %]	552 (527, 579) [+30 %]	571 (544, 599) [+34 %]	551 (525, 578) [+30 %]
ERA5 (*sf*)	624	–	–	–	–	–

Z_e–SR relations. In terms of the sublimation ratio SubR of Sect. 2.6.2, SWE estimated at the 315 m LOH of the most common MRR configuration exceeds the 105 m reference by 20–21 %, and at the EarthCARE-like 490 m by 29–30 %. These four-year percentages average over a substantial year-to-year variability of the blind-zone effect, shown in Appendix D.

475 At the CloudSat-like heights the excess does not continue to grow. It reaches its maximum at 700 m (+34 % for all three relations) and decreases slightly at 945 m (+30 to +31 %), consistent with the four-year mean reflectivity, which stops increas-

https://doi.org/10.5194/egusphere-2026-6639
Preprint. Discussion started: 30 October 2026
© Author(s) 2026. CC BY 4.0 License.

ing with height above about 500 m and decreases by 0.6 dB between 700 and 945 m. For EarthCARE the surface snowfall overestimation due to the BZ at this site is therefore only moderately smaller than for CloudSat (29–30 % against 34 % over the four years).

The sweep can also be extended below the MRR LOH thanks to the Parsivel observations at the ground (see Sect. 2.6.1 and the points at LOH $= 0$ in Fig. 12). Because the Parsivel record of 2021 covers the summer months only, this extension uses three years instead of four (2020, 2023 and 2024). Leaving out 2021 (Table 1) lowers the radar virga share at 105 m from 38.4 to 37.3 % and raises the precipitation share from 58.9 to 60.2 %. Over these three years the virga share rises from 37.3 % at 105 m to 39.9 % at the ground, and the precipitation share decreases correspondingly from 60.2 to 57.5 %. The ground and 105-m shares are close, which indicates that the 105-m gate already captures most of the depletion, and the residual difference is in the direction expected if part of it continues below that height. The same check applied to the accumulation gives a consistent figure. Retaining only the hours with counts at the disdrometer removes 6 % of the SWE estimated at 105 m, for all three Z_e–SR relations and over the three years with disdrometer coverage (0 m column of Table 3). The step from the lowest radar gate to the ground is therefore small compared with the 29 % gained between the EarthCARE-like LOH and 105 m. Under the simplest interpretation, i.e. a satellite radar that assumes the echo at its LOH to reach the ground, this is the direct overestimation of surface snowfall attributable to sublimation below the BZ at this coastal site.

4 Discussion

In this section we review how much the results for *virga* occurrence and snowfall accumulation depend on the height from which the atmosphere is observed, then how they compare with the estimates available at other Antarctic sites and with the reanalysis, and finally what they imply for the observing systems, in orbit and at the ground.

The simulation of satellite BZ effects presented in Sect. 3.5 shows how strongly the virga statistics and the missing precipitation depend on the observation height. Our reference gate (105 m) is remarkably low for the standards of both spaceborne radars and many MRR-2 deployments. The percentages reported in Sect. 3.2 for the MRR are conservative: part of the depletion necessarily continues below 105 m, as suggested by the disdrometer point-wise measurements at surface level, which raise the virga share from 37.3 to 39.9 % over the three years with disdrometer coverage (Sect. 3.5). At CPR-like LOHs, 35–65 % of the virga columns are indistinguishable from precipitation, and the derived surface accumulation is overestimated by 29–30 % (EarthCARE-like LOH) to 34 % (CloudSat-like LOHs) over the four years, with individual years reaching $+55$ %, before any retrieval uncertainty is considered. This is the direct, site-specific quantification of the BZ problem identified for CloudSat over the polar regions by Maahn et al. (2014), and it implies that BZ corrections cannot rely on a single static factor. The effect varies substantially from year to year, and its magnitude at a coastal, katabatic-dominated site like MZS may not be representative of the flatter interior. The same simulation also provides a first site-specific term of comparison between the CloudSat and EarthCARE observation geometries and their effect on the surface snowfall estimation. At MZS, the deeper CloudSat BZ adds a few percentage points of overestimation with respect to the EarthCARE one, a modest but systematic offset that any merged climatology based on the two missions should account for.

https://doi.org/10.5194/egusphere-2026-6639
Preprint. Discussion started: 30 October 2026
© Author(s) 2026. CC BY 4.0 License.

Corrections for the BZ are already applied to the estimates built on CloudSat. In the reconciliation of the satellite snowfall with the mass budget derived from ice discharge and GRACE, Behrangi et al. (2020) adjust the CloudSat accumulation for what happens in the lowest 1.2 km using the vertical profile of the ECMWF IFS, the same forecasting system underlying the ERA5 reanalysis evaluated here, and the adjustment raises the Antarctic mean from 113 to 161 mm yr^{-1}. Its sign is therefore opposite to the one that our measurements imply at MZS. The two results are not in contradiction though, because two processes act in opposite directions within the same layer: (1) shallow precipitation that the satellite does not detect adds to the surface estimate, and is expected to dominate over the interior of Antarctica, while (2) the sublimation of the snow that the satellite does detect aloft subtracts from it, and is what we measure at a coastal site (analyses not shown quantify the shallow term at MZS as an order of magnitude smaller than the sublimation one under the same BZ geometries). A correction factor for the BZ problem obtained from the model usually carries the first term, while the second term is included only to the extent that the model is able to reproduce the near-surface depletion. Our results indicate that at MZS it does not (Sect. 3.4). Which of the two terms prevails, and thus the sign of the correction, is therefore a local question, and answering it requires observations taken inside the layer.

The virga magnitude found at MZS is consistent with the independent estimates available along other margins of East Antarctica. At Davis, the loss of about 50 % of the snowfall mass recalled in Sect. 1 also takes place entirely within the CloudSat BZ, below the snowfall peak at 1.2 km, and the virga there is associated with Föhn conditions in the lee of an upwind ice ridgeline (Alexander et al., 2023). The triggering mechanism differs from the katabatic drainage acting at MZS and DDU (Grazioli et al., 2017), but the two flows share the adiabatic warming and drying of the descending air that sustains sublimation, with the Föhn case adding the upwind removal of moisture by orographic precipitation (Gehring et al., 2022). Taken together, these site-specific estimates are consistent with the continental-scale figures for the coastal margins: a snowfall reduction of up to 35 % on the margins of East Antarctica, from observations and models (Grazioli et al., 2017), and an atmospheric sublimation equal to 26 % of the snowfall reaching the ground over the areas below 1000 m a.s.l. in the regional climate model MAR (Agosta et al., 2019). The second figure is normalised like our overestimation, by the snow that reaches the ground. How far a single figure of this kind can be applied to other sites along the coast is a separate question, since profiler transects show that virga occurrence and the depth of the sub-cloud dry layer change over a few tens of kilometres of complex terrain (Ferrone et al., 2023), and again along the 1100 km that separate the coast from the plateau (Corden et al., 2026, preprint).

The comparison with ERA5 draws a consistent picture of what a state-of-the-art reanalysis does and does not capture at such a site. The thermodynamic environment of the three radar classes is qualitatively well represented: the sub-cloud dry layer during virga hours, the moist column during precipitation, the ordering of cloud bases and the veering from synoptic easterlies aloft to the katabatic westerly outflow near the surface are all present in the reanalysis fields (Figs. 6–8). The surface expression of the katabatic regime, however, is not reproduced. Wind speeds are strongly underestimated and the directional contrast between regimes is blurred. Most importantly for mass-balance applications, the model precipitation is only weakly coupled to this otherwise realistic low-level structure: snow content crosses the dry layer nearly unchanged, surface snowfall is deposited in 90 % of the virga hours, and the resulting accumulation exceeds the whole envelope of the ground-based

https://doi.org/10.5194/egusphere-2026-6639
Preprint. Discussion started: 30 October 2026
© Author(s) 2026. CC BY 4.0 License.

estimates. In our view this cautions against using reanalysis surface snowfall as a reference at coastal Antarctic sites, even where its column thermodynamics verifies well.

Independent evaluations point in the same direction. At DDU, the models and reanalyses assessed during the YOPP Special Observing Period predicted the occurrence of precipitation well, but produced too many precipitating days and overestimated the amount deposited at the surface (Roussel et al., 2023), which is the same combination of a well-captured environment and an excess of surface snowfall that we find at MZS. Earlier comparisons against the accumulation recorded by automatic weather stations had already shown that the ECMWF reanalysis produces both more and larger precipitation events than the other products available at the time, and that none of the reanalyses assessed can be taken as a reference for the surface mass balance on its own (Cohen and Dean, 2013; Liu et al., 2018). The same excess is visible at the continental scale, where the reanalysis exceeds the CloudSat surface snowfall product most markedly along the coastal and ice-shelf sectors (Song et al., 2026). That comparison, however, is made against a reference that does not resolve the layer in which the depletion measured here takes place, and our simulation indicates that a CloudSat-like LOH overestimates the surface accumulation at MZS by about 34 %. The difference between the reanalysis and the snow that actually reaches the ground is therefore likely to be larger than such continental-scale comparisons indicate, at least along the coastal sectors where the low-level sublimation is active.

The reanalysis shows related biases in other near-surface fields at coastal sites. Raman lidar profiling at Neumayer finds a dry bias of about 10 % in the ERA5 lower-tropospheric moisture in winter (Jakob et al., 2026, preprint), in agreement with the -8 to $-11\,\%$ low-level RH difference against the MZS radiosondes (Appendix C), and ceilometer observations at Scott Base show an underestimation of the cloud occurrence below 3 km (McDonald et al., 2025). Both biases point to the representation of the stable polar boundary layer rather than to the large-scale circulation, which is the same conclusion suggested by our comparison, where the reanalysis captures the regime dependence of the column structure but not its near-surface expression.

Our results also outline what it would take to constrain the model, or a BZ-limited satellite retrieval, with information measured inside the layer. Screening ERA5 with the radar classification removes 32–42 % of the annual accumulation, and no single model variable provides an equivalent screening on its own. Filtering ERA5 with its own near-surface snow content retains 96–98 % of the accumulation, and a simple threshold on the snowfall rate cannot reproduce the radar-based screening either (Sect. 3.4). The screening therefore has to come from an observation inside the BZ itself, which is what a site equipped with a low-LOH profiler provides. The clean separation of the three classes in MRR-independent meteorological variables such as RH, wind speed and cloud base height (Fig. 6) suggests, however, that the required information can be obtained through a proper combination of these meteorological variables. These variables are routinely available from weather stations and both reanalyses and operational weather models, hence virtually over every Antarctic coast site. Reconstructing the radar classification from several standard predictors at once, and hence transferring the screening to periods and places without a profiling radar, appears feasible and is the subject of ongoing work.

The same site-level figures also provide insights into the past and future spaceborne records. In the Arctic, the BZ question addressed here has been examined with the KAZR cloud radar at the North Slope of Alaska, with analogous implications for the satellite-derived snowfall statistics (Shates et al., 2025). With CloudSat operations concluded and EarthCARE in orbit, now expected to operate until 2034, the WIVERN mission would complete a sequence of three spaceborne W-band radars

https://doi.org/10.5194/egusphere-2026-6639
Preprint. Discussion started: 30 October 2026
© Author(s) 2026. CC BY 4.0 License.

(Illingworth et al., 2018; Battaglia et al., 2022). Its conically scanning geometry is expected to improve hydrometeor detection near the surface over sea and to worsen it marginally over land and sea ice (Coppola et al., 2025), and strategies to reduce the sampling errors of radar-based snowfall climatologies are being assessed (Scarsi et al., 2025). Ground-based statistics of the kind presented here provide a reference against which these developments can be tested, and, beyond the mass balance, the event-scale context of the isotopic signals that sublimation imprints on the vapour and on the snowpack (Casado et al., 2021; Petteni et al., 2026), now measurable continuously in East Antarctica (Lauwers et al., 2026).

The spatial caveat raised above sets the last point. These results come from a single site, and the profiler transects indicate that the depletion varies over distances much shorter than the coast itself, so generalising them requires similar observations at more locations. The instrumental basis for this already exists, and is collected in Appendix A. MRRs are or have been operated, usually in the coarser 300–3000 m configuration, at DDU (Genthon et al., 2018; Durán-Alarcón et al., 2019; Wiener et al., 2024), Princess Elisabeth (Gorodetskaya et al., 2015; Souverijns et al., 2017; Ferrone and Berne, 2023), Davis (Alexander et al., 2023), Concordia (Di Natale et al., 2018, 2022), at Neumayer, where the MRR record has been running since 2019 and was recently complemented by the one-year COALA remote-sensing campaign (Radenz et al., 2024), and, more recently, at Great Wall research station on the Antarctic Peninsula (Sun et al., 2026). A growing number of these records is openly available (e.g. Wiener et al., 2024; Ferrone and Berne, 2023; Schmithüsen, 2025; Roversi et al., 2026b). The classification itself requires nothing beyond the radar profiles, so it can be applied to any of these records as they stand, while a co-located disdrometer, common at the same stations, adds the surface term that closes the profile at the ground and makes the residual depletion below the LOH measurable. The MRR–disdrometer pair can run unattended year-round at low power, without field calibration and at a cost well below that of scanning or higher-frequency systems. A coordinated assessment of near-surface sublimation around the continent is therefore a concrete possibility, and one that fits the observational strategy of Antarctica InSync (Schmale et al., 2026), which gives priority to what can be built on the long-term records already running. Those records provide the basis, and the present work adds a classification that turns their profiles into a statistic on how much of the snowfall reaches the ground.

5 Conclusions

Four years of vertically pointing K-band radar observations at Mario Zucchelli Station were used to classify 5-min profiles into *precipitation*, *virga* or *noisy*, based on whether hydrometeor echoes reach the lowest reliable gate (105 m), and to quantify what the resulting near-surface sublimation implies for the satellite radars and reanalyses that cannot observe these heights, such as the CPR on board EarthCARE.

Virga is a persistent feature of the MZS record: 38 % of the hydrometeor-bearing columns produce no echo at 105 m, and the share holds in all four years (33–43 %). The classes correspond to distinct meteorological regimes in models and observations that carry no radar information (surface humidity, ceilometer-reported height (CRH), cloud base height from the reanalysis, and the synoptic-versus-katabatic wind circulation), identifying the katabatic-driven sub-cloud dry layer as the environment in which coastal snowfall is depleted.

https://doi.org/10.5194/egusphere-2026-6639
Preprint. Discussion started: 30 October 2026
© Author(s) 2026. CC BY 4.0 License.

Simulating progressively higher lowest observable heights (LOH) shows that a CPR-like observation geometry misclassifies 35–65 % of the virga columns as precipitation and overestimates the four-year surface accumulation by 29–30 % at the EarthCARE-like LOH and by up to 34 % at the CloudSat-like LOHs, with individual years reaching +55 %. Blind-zone effects at this site are large, year-dependent, and cannot be removed by a single static correction factor. Their magnitude is consistent with the estimates available at other East Antarctic sites, from Dumont d'Urville to Davis, and with the continental-scale estimates of the coastal sublimation from observations and regional climate modelling (Sect. 4). The simulation also quantifies the offset between the CloudSat and EarthCARE observation geometries at this site, a prerequisite for connecting the two non-overlapping satellite records.

ERA5 reproduces the thermodynamic environment of the virga regime but not its consequence: model snow crosses the dry layer, surface snowfall is deposited in 90 % of the virga hours, and the four-year accumulation (624 mm) exceeds the entire range of the MRR-based estimates (213–425 mm). Screening the reanalysis with the radar classification removes 32–42 % of the annual accumulation, and no single model variable provides an equivalent screening. The model's own near-surface snow content retains 96–98 % of the accumulation, and no simple snowfall-rate threshold reproduces the radar-based selection.

The numbers above carry their own limits. They isolate the bias hidden in the sampling geometry, without addressing the specific uncertainties of the spaceborne retrievals. While the occurrence bias is characterised consistently across the record, the microphysical uncertainty of the ground-based estimate dominates the spread of the accumulation, and the year-to-year range in Appendix D is of the same order. The transects discussed in Sect. 4 set the remaining limit, since a site-level figure does not transfer unchanged along the coast.

Taken together, these results establish MZS as a process-based reference for the interpretation of blind-zone-affected snowfall products in coastal East Antarctica. The observed regime separation in standard meteorological variables indicates a practical way forward, namely reconstructing the radar classification from those variables alone, so that the screening applied here can be transferred to periods and locations without a profiling radar. With EarthCARE now in orbit, the present record also provides the ground-based term of comparison for its snowfall estimates over this sector of coastal Antarctica. The growing network of MRR-equipped Antarctic stations, with an increasing number of openly available records, makes a coordinated assessment of near-surface sublimation around the continent a concrete next step, and one that would establish how much the effect varies from site to site along the East Antarctic coast, and whether it holds on the Antarctic Peninsula and in West Antarctica, where records are now starting to accumulate. Site-level statistics of this kind will keep their role as the ground reference for the current and the next generation of spaceborne W-band radars, such as WIVERN.

https://doi.org/10.5194/egusphere-2026-6639
Preprint. Discussion started: 30 October 2026
© Author(s) 2026. CC BY 4.0 License.

Appendix A: Antarctic records of profiling radars and disdrometers

This appendix supports the argument of Sect. 4 that the assessment carried out here could be repeated elsewhere. Table A1 lists the Antarctic deployments of profiling radars and disdrometers known to us, and Fig. A1 shows where they are.

Eleven of the twelve records come from an MRR, in the MRR-2 or the MRR-PRO version, and the remaining one from the KAZR cloud radar operated at McMurdo during the AWARE campaign (Lubin et al., 2020). A disdrometer is co-located in six of them. Eight records are openly available and one more up to 2019.

The coverage is uneven. The deployments concentrate along the coast, the interior being represented by Concordia alone, and three of them are on the Antarctic Peninsula, two a few kilometres apart on King George Island. Terra Nova Bay hosts two independent deployments, the ENEA one behind the Scarchilli et al. (2020) relation and the CNR-ISAC one used here. Ship-borne campaigns over the Southern Ocean are not included.

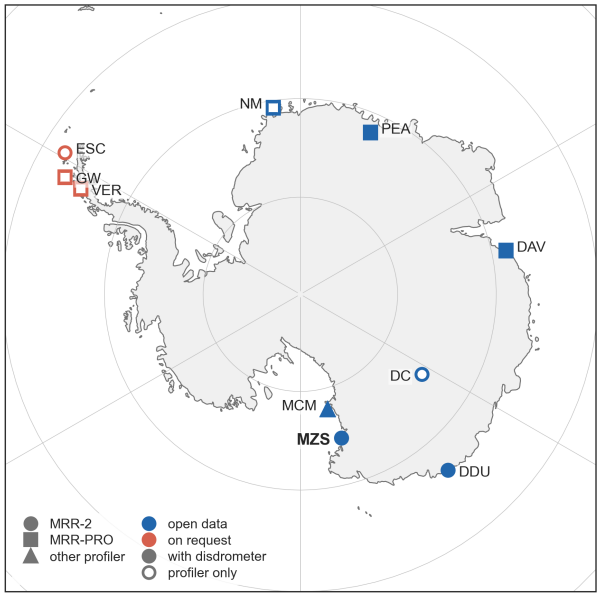

Figure A1. Antarctic sites with a profiling radar or a disdrometer record. Labels are the codes of Table A1, where the sites are named. Colour: whether the data are openly available or provided on request. Marker: MRR-2 (circle), MRR-PRO (square) or another profiler (triangle). Filled markers indicate a co-located disdrometer. Deployments sharing a site are drawn as a single marker, which is the case for the two Mario Zucchelli records and for the two Princess Elisabeth ones. Escudero and Great Wall keep separate markers, being operated by different teams, and are drawn one above the other because the two stations stand a few kilometres apart on King George Island.

https://doi.org/10.5194/egusphere-2026-6639
Preprint. Discussion started: 30 October 2026
© Author(s) 2026. CC BY 4.0 License.

Table A1. Antarctic station deployments of profiling radars and disdrometers, from north to south. Codes are those of Fig. A1. Periods are those documented by the references listed.

Code	Site	Coordinates	Period	Radar	Disdrometer	Data	Reference
ESC	Escudero (King George I.)	62.2° S, 59.0° W	2022–today	MRR-2	–	on request	Hines et al. (2026)
GW	Great Wall (King George I.)	62.2° S, 59.0° W	2024–2026	MRR-PRO[a]	–	on request	Sun et al. (2026)
VER	Vernadsky	65.2° S, 64.3° W	2022–today	MRR-PRO	–	on request	Hines et al. (2026)
DDU	Dumont d'Urville	66.7° S, 140.0° E	2015–today	MRR-2	MASC, VPF-730	open	Genthon et al. (2018)
							Durán-Alarcón et al. (2019)
							Wiener et al. (2024)
DAV	Davis	68.6° S, 78.0° E	2018–2019	MRR-PRO	MASC	open	Alexander et al. (2023)
NM	Neumayer III	70.7° S, 8.3° W	2019–today	MRR-PRO	–	open	Schmithüsen (2025)
							Radenz et al. (2024)
PEA	Sør Rondane transect	72.0° S, 23.4° E	2019/2020	3x MRR-PRO	MASC[b]	open	Ferrone and Berne (2023)
							Ferrone et al. (2023)
PEA	Princess Elisabeth	72.0° S, 23.4° E	2010–2019	MRR-2	PIP	open	Gorodetskaya et al. (2015)
							Souverijns et al. (2017)
MZS	Mario Zucchelli, Climantartide	74.7° S, 164.1° E	2015–today	MRR-2	LPM	open[c]	Scarchilli et al. (2020)
MZS	Mario Zucchelli, APP	74.7° S, 164.1° E	2019–today	MRR-2	Parsivel, 3DS	open	Bracci et al. (2022a)
							Roversi et al. (2026b)
							Roversi et al. (2026a)
DC	Concordia (Dome C)	75.1° S, 123.3° E	2019–today	MRR-2	LPM[b]	open	Di Natale et al. (2018)
MCM	McMurdo	77.8° S, 166.7° E	2015–2016	KAZR	Parsivel	open	Lubin et al. (2020)
							Tridon et al. (2022)

[a] model not stated by the authors, inferred from the 128 range gates. [b] disdrometer on site but not co-located with the radar. [c] open until 2019, on request afterwards.

Appendix B: ERA5 grid-point selection at MZS

Section 2 introduced the single 0.25° cell used as the MZS proxy, centred at 74.75° S, 164.0° E (Fig. B1), together with its coastal-mixed character (land fraction 0.55) and its model orography (the surface geopotential height z/g_0) of 108 m, some 88 m above the real 20 m instrument elevation. That mismatch reflects the terrain rather than an unfortunate choice. Across the 3×3 neighbourhood downloaded around the station the model orography ranges from -31 m (Terra Nova Bay, to the south) to 587 m (the Northern Foothills, to the north) and the land fraction from 0.11 to 0.88. This appendix reports in detail why the single containing cell is retained and how sensitive the results of the paper are to that choice.

To decide whether the containing cell, or some neighbourhood average, best represents the station, the Eneide AWS (Sect. 2) is used as an independent arbiter. The AWS stands at 91 m a.s.l., about 0.7 km from the profiling instruments and some 71 m above their deck, so it samples the same coastal site from slightly higher up. Three estimators (the nearest cell, the mean of the four grid points at the vertices of the cell containing the station, and a bilinear interpolation to the station location) are scored against the hourly observations. The nearest cell performs best for every field, and decisively so for surface pressure, the cleanest elevation discriminator. The nearest cell nearly matches the station ($r = 0.99$, bias -2 hPa, consistent with the 17 m by which the model orography exceeds the AWS elevation), whereas the four-point mean is 26 hPa low because it blends in the cold, elevated inland cells to the north (the same reason it degrades the 2-m temperature). Spatial averaging therefore

https://doi.org/10.5194/egusphere-2026-6639
Preprint. Discussion started: 30 October 2026
© Author(s) 2026. CC BY 4.0 License.

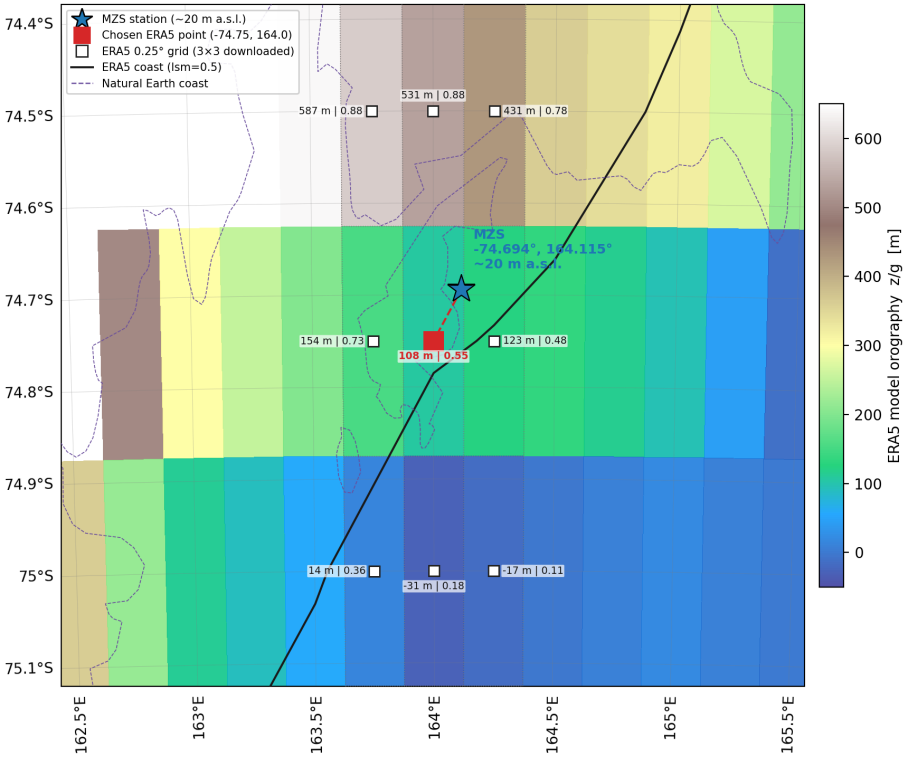

Figure B1. Locator map of the ERA5 grid point used as the MZS proxy. Background: ERA5 model orography (z/g_0); solid black line: the model's own coastline (land fraction $= 0.5$); dashed line: Natural Earth coastline. The chosen cell (red square, 7.1 km from the station) contains the station (star); each grid point of the downloaded 3×3 neighbourhood is labelled with its model orography and land fraction.

worsens the representation rather than improving it, and the single nearest cell is retained. Wind direction is reproduced poorly by all three estimators alike. The error, resolved by hour of day, swings by $\sim$27° identically for the three, consistent with an unresolved diurnal veering of the katabatic flow rather than with the grid-point choice.

The remaining question is whether the results of Sects. 3.2 and 3.3 depend on the chosen pixel. Scanning the spatial spread of each field across the nine cells separates the fields into two groups: the dynamical boundary-layer quantities, which vary strongly from cell to cell (coefficient of variation of 50–58 % for boundary-layer height and for the 10-m and 975-hPa winds; skin-temperature standard deviation of $\sim$7.5 °C), and the quantities that carry the conclusions of this paper, which are nearly uniform across the 3×3 neighbourhood. The annual snowfall accumulation and the column snow content have coefficients of variation of 3.7 and 3.5 % respectively. The spread of the fragile fields is, moreover, understood rather than random. Regressing the nine values of each field on land fraction and model orography explains $R^2 \sim 0.9$–1.0 of their spatial variance, i.e. the proxy uncertainty is the Terra Nova Bay coastal transition itself.

Two checks confirm that the headline findings do not hinge on the pixel. First, the weak-sublimation signature of Sect. 3.2.2 is reproduced at every cell. In the MRR-virga hours with ERA5 snow at 850 hPa ($cswc > 10^{-3}$ g kg^{-1}, as in Fig. 9), the

https://doi.org/10.5194/egusphere-2026-6639
Preprint. Discussion started: 30 October 2026
© Author(s) 2026. CC BY 4.0 License.

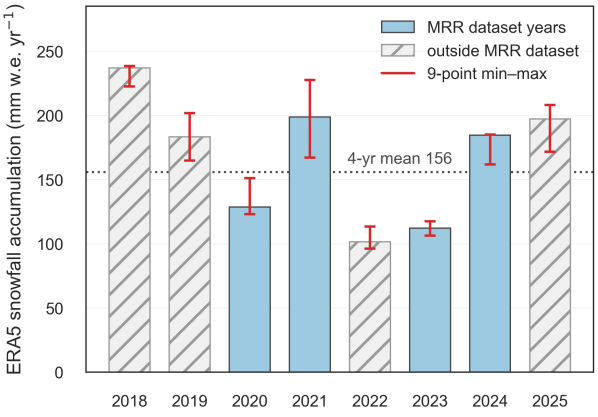

Figure B2. ERA5 annual snowfall accumulation at MZS: the chosen grid point (bars) against the min–max spread of the 3×3 neighbourhood (whiskers). Hatched bars: years outside the MRR dataset (from monthly-mean ERA5 fields), shown for context. The spatial band ($\pm 3.7\,\%$ on the four-year mean) is far narrower than the interannual variability.

snow content at the pressure level that lies at the model surface is lower than at 850 hPa in $79 \pm 3\,\%$ of the hours. Yet ERA5 still deposits snow at the ground (snowfall rate above 10^{-4} mm h^{-1}, as in Sect. 3.2.2) in $91 \pm 1\,\%$ of the virga hours. Both values are the mean and standard deviation over the nine cells (82 and 90 % at the chosen cell), so the behaviour belongs to the model over the whole coastal area, not to the chosen point. Second, the ERA5 annual snowfall accumulation carries a spatial-representativeness band of only $\pm 3.7\,\%$ (± 6 mm yr^{-1} on a four-year mean of 156 mm yr^{-1}), an order of magnitude smaller than its interannual range (112–199 mm yr^{-1} over the four MRR years, and 102–237 mm yr^{-1} over the extended 2018–2025 context of Fig. B2, whose driest year is 2022, the year of the MRR gap). The MRR-based filtering of Sect. 3.4, being multiplicative, inherits this small band.

Appendix C: Radiosonde assessment of the ERA5 column

An independent observed view of the thermodynamic column is provided by the operational radiosoundings performed at MZS by the Italian Antarctic Meteo-Climatological Observatory (Grigioni et al., 2022c). The soundings resolve temperature, pressure, humidity and wind at ∼5 m vertical spacing and are launched once or twice per day at the 00 and 12 UTC synoptic hours during the summer campaigns, essentially October to January (Fig. C1). Over the four project years this yields 628 launches (154, 170, 156 and 148 in 2020, 2021, 2023 and 2024 respectively), essentially all of which reach the 500-hPa level. Two checks are built on this dataset: a validation of the ERA5 pressure-level profiles used in Sect. 3.2, and an observed counterpart of the per-class composites of Fig. 8. The seasonal sampling must be kept in mind: both checks characterise the summer column only.

https://doi.org/10.5194/egusphere-2026-6639
Preprint. Discussion started: 30 October 2026
© Author(s) 2026. CC BY 4.0 License.

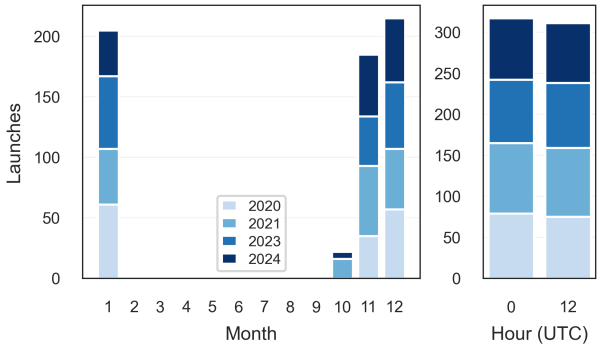

Figure C1. Monthly and nominal-hour distribution of the 628 radiosonde launches at MZS over the four project years, stacked by year. The soundings sample the summer campaigns only, essentially October to January.

The comparison is performed at launch times. Each sounding is paired with the ERA5 profile of its nominal hour at the grid point of Appendix B, and its samples are averaged onto the eleven ERA5 pressure levels using layers delimited by the geometric midpoints between adjacent levels. With one or two launches per day, no denser temporal pairing is involved. The 1000-hPa level lies below the station-level surface pressure (∼985 hPa) for all but 29 launches and is excluded. One convention difference matters for humidity. The radiosonde reports relative humidity with respect to liquid water at all temperatures, whereas ERA5 archives pressure-level relative humidity with respect to a mixed water–ice saturation, blending quadratically between water saturation at $0\,^{\circ}\mathrm{C}$ and ice saturation at $-23\,^{\circ}\mathrm{C}$ (ECMWF, 2016). ERA5 values are therefore converted to the radiosonde convention as

$$\mathrm{RH_w} = r\,\frac{\alpha\, e_{\mathrm{s,w}}(T) + (1-\alpha)\, e_{\mathrm{s,i}}(T)}{e_{\mathrm{s,w}}(T)}, \tag{C1}$$

where the weight given to water saturation is

$$\alpha = \left[\max\left(0, \min\left(1, \frac{T - T_{\mathrm{i}}}{T_0 - T_{\mathrm{i}}}\right)\right)\right]^2, \tag{C2}$$

with $T_0 = 273.16$ K, $T_{\mathrm{i}} = 250.16$ K and the saturation vapour pressures over water and ice, $e_{\mathrm{s,w}}$ and $e_{\mathrm{s,i}}$, from the Magnus approximations of Alduchov and Eskridge (1996). The correction is negligible near the surface but grows with altitude as temperature decreases. Without it, the comparison at 500 hPa would show a spurious moist bias of about $+18\,\%$ (dashed line in Fig. C2a).

C1 Column bias at launch times

Figure C2 shows the ERA5-minus-sonde difference profiles. Temperature is closely reproduced. The median bias stays within $\pm 0.9\,^{\circ}\mathrm{C}$ at all levels and per-level correlations are 0.97 or higher. The wind components show small biases (within $\pm 0.7\ \mathrm{m\,s^{-1}}$ above 900 hPa), with a moderate positive zonal offset of about $+1.2\ \mathrm{m\,s^{-1}}$ in the lowest levels, where the katabatic outflow

https://doi.org/10.5194/egusphere-2026-6639
Preprint. Discussion started: 30 October 2026
© Author(s) 2026. CC BY 4.0 License.

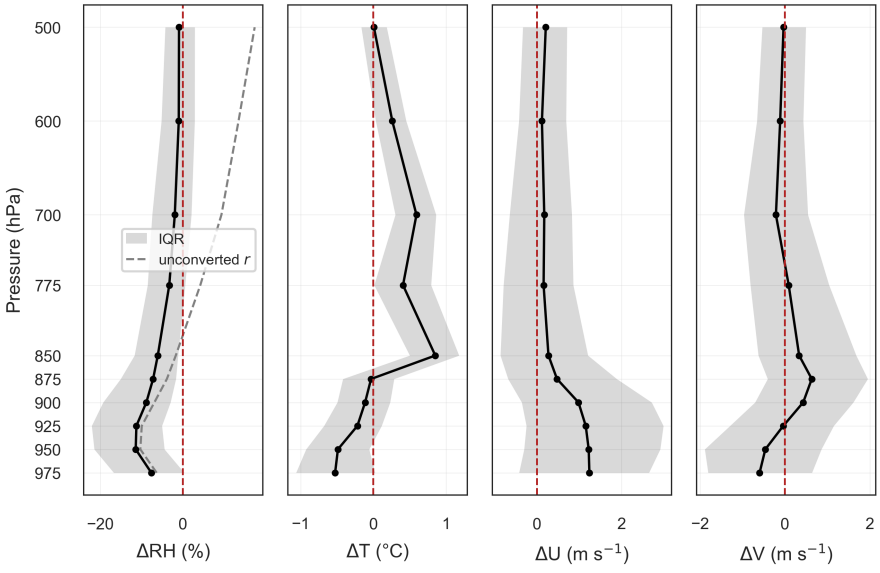

Figure C2. ERA5-minus-radiosonde difference profiles at launch times (628 launches, 2020–2024 excluding 2022; median and interquartile range): relative humidity (after conversion to the over-liquid convention, Eq. C1), temperature, and zonal (U) and meridional (V) wind components. The grey dashed line shows the median RH difference if the archived mixed-phase r is compared directly with the sonde. The 1000-hPa level, below the surface for all but 29 launches, is excluded.

dominates. Relative humidity is where ERA5 departs most from the observations. The reanalysis is drier than the sonde in the boundary layer, with a median difference of -8 to $-11\,\%$ between 975 and 900 hPa that decays to about $-1\,\%$ at 500 hPa. Per-level scatterplots (not shown) indicate that this dry difference is concentrated in the moderately sub-saturated cases (sonde RH of 40–80 %), while near-saturated profiles lie close to the one-to-one line. The vertical structure of the summer column is therefore well captured, with the caveat that ERA5 tends to overstate the sub-saturation of an already dry boundary layer, a bias to keep in mind when reading the absolute RH levels of Fig. 8, and one that does not affect the classification-based statistics of Sect. 3.2, which never use ERA5 humidity as input.

C2 Radiosonde composites by MRR class

Grouping the launches by the MRR class of their hour (44 precipitation, 32 virga and 525 no-signal launches, the remaining 27 falling in hours for which no MRR class is available) provides an observed counterpart of the ERA5 composites of Fig. 8, shown in Fig. C3. The sample is small, and the medians should be read as indicative, but the environment separation of Sect. 3.2 is reproduced by the soundings alone: precipitation launches are moist through the column (median RH around or above 90 % between 925 and 775 hPa), virga launches track the precipitation composite in the mid levels but dry markedly below 850 hPa, down to a median RH of ∼61 % at 975 hPa (the moderately sub-saturated low layer in which falling snow sublimates), and no-signal launches are drier at all levels (median RH below 52 %). The ERA5 medians at the same launch times (dashed)

https://doi.org/10.5194/egusphere-2026-6639
Preprint. Discussion started: 30 October 2026
© Author(s) 2026. CC BY 4.0 License.

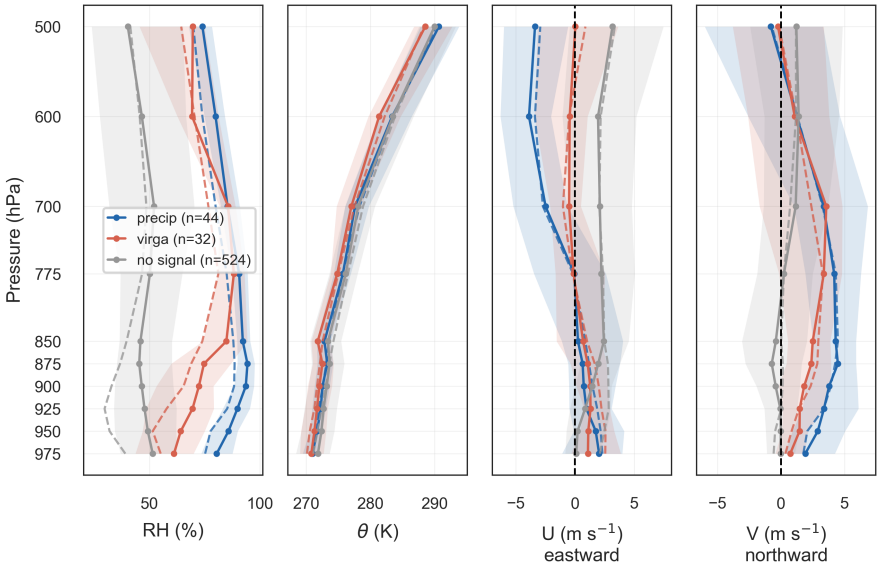

Figure C3. Radiosonde composites by MRR class at launch time (solid: median; shading: interquartile range): relative humidity, potential temperature θ, and zonal (U) and meridional (V) wind components. Dashed lines: ERA5 medians at the same launch times. Levels sampled by fewer than 10 launches of a class are not drawn.

follow the sonde composites closely for the precipitation and virga classes, consistent with the dry difference of Fig. C2 being concentrated in the intermediate-humidity, largely no-signal population.

Appendix D: Snowfall-rate relations and per-year accumulation tables

Table D1 lists the coefficients of the Z_e–SR power laws used to convert reflectivity into snowfall rate (Sect. 2.5), with the uncertainty ranges propagated by Monte Carlo into the accumulation envelopes reported throughout Sect. 3.3.

Table D2 repeats the blind-zone assessment of Table 3 for the individual years. The vertical structure of the effect is the same in all years (the excess over the 105-m reference grows with the simulated LOH, peaks at the CloudSat-like 700 m and decreases

Table D1. Coefficients of the power-law Z_e–SR relations used in this study, in the form $Z_e = a\,\mathrm{SR}^b$ with Z_e in $\mathrm{mm^6\,m^{-3}}$ and SR in $\mathrm{mm\,h^{-1}}$ of snow water equivalent. Parentheses give the 5th–95th percentile range of each coefficient.

Relation	Source	a	b
Bracci (Aggregates)	Bracci et al. (2022a)	134 (122, 146)	1.25 (1.17, 1.32)
Bracci (Pristine)	Bracci et al. (2022a)	95 (85, 107)	1.18 (1.12, 1.25)
Scarchilli	Scarchilli et al. (2020)	54 (51, 56)	1.15 (1.13, 1.17)

https://doi.org/10.5194/egusphere-2026-6639
Preprint. Discussion started: 30 October 2026
© Author(s) 2026. CC BY 4.0 License.

Table D2. As Table 3, but for the individual years. The 0 m column is empty for 2021, the year whose Parsivel record covers the summer months only. Over the other three years the ground check removes less than 0.1 % of the accumulation in 2020 and 2023 and 14 % in 2024, mostly in three January events. Over the three years together the change is −6 % (Table 3).

Year	Relation	0 m (surface)	105 m	315 m	490 m	700 m	945 m
2020	Bracci (Aggr.)	40 (35, 45) [0 %]	40 (35, 45)	48 (43, 54) [+21 %]	53 (46, 59) [+32 %]	54 (48, 61) [+36 %]	52 (46, 59) [+31 %]
	Bracci (Pris.)	50 (43, 57) [0 %]	50 (43, 57)	61 (53, 69) [+22 %]	66 (57, 75) [+32 %]	68 (59, 77) [+36 %]	64 (56, 73) [+29 %]
	Scarchilli	79 (76, 83) [0 %]	79 (76, 84)	97 (92, 102) [+22 %]	105 (100, 111) [+33 %]	108 (103, 114) [+36 %]	102 (97, 107) [+28 %]
	ERA5 (*sf*)	128	–	–	–	–	–
2021	Bracci (Aggr.)	–	77 (69, 86)	90 (80, 100) [+17 %]	94 (83, 105) [+21 %]	96 (85, 108) [+24 %]	94 (83, 106) [+22 %]
	Bracci (Pris.)	–	98 (86, 110)	115 (101, 130) [+17 %]	119 (105, 134) [+22 %]	121 (106, 138) [+24 %]	118 (103, 134) [+21 %]
	Scarchilli	–	157 (150, 165)	185 (177, 194) [+18 %]	191 (183, 201) [+22 %]	195 (186, 204) [+24 %]	189 (180, 198) [+20 %]
	ERA5 (*sf*)	199	–	–	–	–	–
2023	Bracci (Aggr.)	42 (37, 48) [0 %]	42 (37, 48)	53 (46, 60) [+26 %]	59 (52, 67) [+42 %]	63 (56, 71) [+51 %]	63 (55, 71) [+50 %]
	Bracci (Pris.)	51 (44, 59) [0 %]	51 (44, 59)	65 (57, 74) [+27 %]	74 (64, 84) [+44 %]	79 (69, 89) [+54 %]	77 (68, 88) [+51 %]
	Scarchilli	81 (77, 85) [0 %]	81 (77, 85)	103 (98, 108) [+27 %]	117 (112, 123) [+45 %]	125 (119, 131) [+55 %]	123 (117, 129) [+52 %]
	ERA5 (*sf*)	112	–	–	–	–	–
2024	Bracci (Aggr.)	47 (41, 52) [−14 %]	54 (48, 60)	64 (57, 72) [+19 %]	69 (61, 77) [+28 %]	72 (64, 81) [+33 %]	70 (61, 79) [+29 %]
	Bracci (Pris.)	58 (51, 65) [−14 %]	68 (60, 76)	81 (71, 91) [+20 %]	86 (76, 97) [+28 %]	89 (79, 101) [+33 %]	86 (75, 98) [+28 %]
	Scarchilli	92 (88, 97) [−14 %]	108 (103, 113)	129 (123, 135) [+20 %]	138 (132, 145) [+28 %]	143 (136, 149) [+32 %]	137 (131, 143) [+27 %]
	ERA5 (*sf*)	185	–	–	–	–	–

slightly at 945 m), but its amplitude varies substantially. At 700 m the excess ranges from $+24\,\%$ in 2021 to $+51\,\%$ in 2023 for Bracci Aggregates, and reaches $+55\,\%$ in 2023 with the Scarchilli et al. (2020) relation, the other Z_{e}–SR relations giving the same year ranking. The four-year percentages of Sect. 3.5 therefore average over a markedly year-dependent quantity, and single-season assessments, such as the preliminary 2023 values of Roversi et al. (2026c), which fall on the high side of this range, should be read accordingly.

Code and data availability. The observations analysed here are openly available as monthly netCDF archives: the MRR-2 vertical profiles at https://doi.org/10.5281/zenodo.22923006 (Roversi et al., 2026b) and the Parsivel size and velocity distributions at https://doi.org/10.5281/zenodo.22922844 (Roversi et al., 2026a), both described by the metadata records of the Italian Antarctic Data Center (Baldini et al., 2025). The near-surface meteorological observations, the ceilometer records and the radiosoundings are distributed by the Italian Antarctic Meteo-Climatological Observatory https://www.climantartide.it/ (Grigioni et al., 2022a, b, c). The ERA5 reanalysis is available from the Copernicus Climate Change Service Climate Data Store (Hersbach et al., 2020). The classification of the radar profiles and the blind-zone simulation are released as the Python package snowreach at https://doi.org/10.5281/zenodo.23087597 (Roversi, 2026), which reproduces the accumulations of Table 3 from the archived MRR files.

https://doi.org/10.5194/egusphere-2026-6639
Preprint. Discussion started: 30 October 2026
© Author(s) 2026. CC BY 4.0 License.

Author contributions. **Giacomo Roversi**: Conceptualization, Methodology, Software, Data Curation, Writing – original draft, Visualization. **Alessandro Bracci**: Conceptualization, Methodology, Validation, Writing – review & editing. **Hajime Okamoto**: Conceptualization, Methodology, Validation, Writing – review & editing, Supervision. **Kaori Sato**: Conceptualization, Methodology, Validation, Writing – review & editing, Supervision. **Luca Baldini**: Conceptualization, Methodology, Validation, Writing – review & editing, Supervision, Funding acquisition.

Competing interests. At least one of the (co-)authors is a guest member of the editorial board of Atmospheric Measurement Techniques for the special issue "Early results from EarthCARE (AMT/ACP/GMD inter-journal SI)". The authors have no other competing interests to declare.

Acknowledgements. This work was supported partially by the Collaborative Research Program of the Research Institute for Applied Mechanics (RIAM), Kyushu University (Adoption 26EA_7 and Project 2024EC-EA-1: "Long-term Statistics of Snowfall Microphysical Features for EarthCARE Validation Activities"), by a PhD scholarship funded by CNR with the support of the National Programme for Research in the Antarctic (PNRA) (CUP H73C23000530005), within the National Doctoral Degree Programme in Polar Sciences coordinated by Ca' Foscari University of Venice, and by the Italian Space Agency (ASI) through the EC-ValMed.it Project under Grant 2023-00-HB.0. This work was also supported by JSPS KAKENHI Grant Number JP24H00275 and by the Japan Aerospace Exploration Agency (EORA4) for the EarthCARE mission. MRR-2 and Parsivel data at MZS were collected within the PNRA funded project "Antarctic Precipitation Properties" (APP). The authors thank ENEA (Antarctic Technical Unit, UTA) and PNRA for the technical and logistic support at MZS, and the Italian Antarctic Meteo-Climatological Observatory Climantartide (https://www.climantartide.it/). The authors used a generative AI language model (Claude Opus 5.5, developed by Anthropic, through Claude Code) in developing the analysis code and in revising the English of this manuscript.

https://doi.org/10.5194/egusphere-2026-6639
Preprint. Discussion started: 30 October 2026
© Author(s) 2026. CC BY 4.0 License.

References

Adirosi, E., Baldini, L., Roberto, N., Gatlin, P., and Tokay, A.: Improvement of Vertical Profiles of Raindrop Size Distribution from Micro Rain Radar Using 2D Video Disdrometer Measurements, Atmospheric Research, 169, 404–415, https://doi.org/10.1016/j.atmosres.2015.07.002, 2016.

Adirosi, E., Baldini, L., and Tokay, A.: Rainfall and DSD Parameters Comparison between Micro Rain Radar, Two-Dimensional Video and Parsivel2 Disdrometers, and S-Band Dual-Polarization Radar, Journal of Atmospheric and Oceanic Technology, 37, 621–640, https://doi.org/10.1175/JTECH-D-19-0085.1, 2020.

Agosta, C., Amory, C., Kittel, C., Orsi, A., Favier, V., Gallée, H., Van Den Broeke, M. R., Lenaerts, J. T. M., Van Wessem, J. M., Van De Berg, W. J., and Fettweis, X.: Estimation of the Antarctic Surface Mass Balance Using the Regional Climate Model MAR (1979–2015) and Identification of Dominant Processes, The Cryosphere, 13, 281–296, https://doi.org/10.5194/tc-13-281-2019, 2019.

Alduchov, O. A. and Eskridge, R. E.: Improved Magnus Form Approximation of Saturation Vapor Pressure, Journal of Applied Meteorology, 35, 601–609, https://doi.org/10.1175/1520-0450(1996)035<0601:IMFAOS>2.0.CO;2, 1996.

Alexander, S. P., Protat, A., Berne, A., and Ackermann, L.: Radar-Derived Snowfall Microphysical Properties at Davis, Antarctica, Journal of Geophysical Research: Atmospheres, 128, e2022JD038 389, https://doi.org/10.1029/2022JD038389, 2023.

American Meteorological Society: Virga (AMS Glossary), AMS Glossary, https://glossary.ametsoc.org/wiki/virga/, last access: 13 October 2026, 2015.

Argentini, S. and Mastrantonio, G.: Barrier Winds Recorded during Two Summer Antarctic Campaigns and Their Interaction with the Katabatic Flows as Observed by a Tri-Axial Doppler Sodar, International Journal of Remote Sensing, 15, 455–466, https://doi.org/10.1080/01431169408954086, 1994.

Arndt, S., Haumann, A., Boetius, A., Aaboe, S., et al.: Antarctica InSync Science Plan, Tech. rep., Scientific Committee on Antarctic Research, https://doi.org/10.67382/EACD5221, 2026.

Baldini, L., Bracci, A., and Roversi, G.: APP (YOPP): Antarctic Precipitation Properties from Ground-Based Instruments, Dataset, Italian Antarctic Data Center (IANDC), https://iandc.pnra.aq/srv/eng/catalog.search#/metadata/dc941200-9195-47db-9e94-ef3acd115869, CC BY-NC-SA 4.0, 2025.

Battaglia, A. and Panegrossi, G.: What Can We Learn from the CloudSat Radiometric Mode Observations of Snowfall over the Ice-Free Ocean?, Remote Sensing, 12, 3285, https://doi.org/10.3390/rs12203285, 2020.

Battaglia, A., Rustemeier, E., Tokay, A., Blahak, U., and Simmer, C.: PARSIVEL Snow Observations: A Critical Assessment, Journal of Atmospheric and Oceanic Technology, 27, 333–344, https://doi.org/10.1175/2009JTECHA1332.1, 2010.

Battaglia, A., Martire, P., Caubet, E., Phalippou, L., Stesina, F., Kollias, P., and Illingworth, A.: Observation Error Analysis for the WInd VElocity Radar Nephoscope W-Band Doppler Conically Scanning Spaceborne Radar via End-to-End Simulations, Atmospheric Measurement Techniques, 15, 3011–3030, https://doi.org/10.5194/amt-15-3011-2022, 2022.

Behrangi, A., Gardner, A. S., and Wiese, D. N.: Comparative Analysis of Snowfall Accumulation over Antarctica in Light of Ice Discharge and Gravity Observations from Space, Environmental Research Letters, 15, 104 010, https://doi.org/10.1088/1748-9326/ab9926, 2020.

Beynon, R. and Hocke, K.: Snow Virga above the Swiss Plateau Observed by a Micro Rain Radar, Remote Sensing, 14, 890, https://doi.org/10.3390/rs14040890, 2022.

https://doi.org/10.5194/egusphere-2026-6639
Preprint. Discussion started: 30 October 2026
© Author(s) 2026. CC BY 4.0 License.

Bracci, A., Baldini, L., Roberto, N., Adirosi, E., Montopoli, M., Scarchilli, C., Grigioni, P., Ciardini, V., Levizzani, V., and Porcù, F.: Quantitative Precipitation Estimation over Antarctica Using Different Ze-SR Relationships Based on Snowfall Classification Combining Ground Observations, Remote Sensing, 14, 82, https://doi.org/10.3390/rs14010082, 2022a.

Bracci, A., Baldini, L., Roberto, N., Adirosi, E., Montopoli, M., Scarchilli, C., Grigioni, P., Ciardini, V., Levizzani, V., and Porcù, F.: Evidence of Sublimation in the Vertical Profiles of Radar Reflectivity and Its Impact on Snowfall Estimation at the Ground at Mario Zucchelli Antarctic Station, in: 2022 3rd URSI Atlantic and Asia Pacific Radio Science Meeting (at-AP-RASC), pp. 1–4, https://doi.org/10.23919/AT-AP-RASC54737.2022.9814266, 2022b.

Bracci, A., Sato, K., Baldini, L., Porcù, F., and Okamoto, H.: Development of a Methodology for Evaluating Spaceborne W-Band Doppler Radar by Combined Use of Micro Rain Radar and a Disdrometer in Antarctica, Remote Sensing of Environment, 294, 113 630, https://doi.org/10.1016/j.rse.2023.113630, 2023.

Bromwich, D. H., Guo, Z., Bai, L., and Chen, Q.-s.: Modeled Antarctic Precipitation. Part I: Spatial and Temporal Variability, Journal of Climate, 17, 427–447, https://doi.org/10.1175/1520-0442(2004)017<0427:MAPPIS>2.0.CO;2, 2004.

Camplani, A., Casella, D., Sanò, P., and Panegrossi, G.: The High lAtitude sNowfall Detection and Estimation aLgorithm for ATMS (HANDEL-ATMS): A New Algorithm for Snowfall Retrieval at High Latitudes, Atmospheric Measurement Techniques, 17, 2195–2217, https://doi.org/10.5194/amt-17-2195-2024, 2024.

Casado, M., Landais, A., Picard, G., Arnaud, L., Dreossi, G., Stenni, B., and Prié, F.: Water Isotopic Signature of Surface Snow Metamorphism in Antarctica, Geophysical Research Letters, 48, https://doi.org/10.1029/2021GL093382, 2021.

Chellini, G., Gierens, R., and Kneifel, S.: Ice Aggregation in Low-Level Mixed-Phase Clouds at a High Arctic Site: Enhanced by Dendritic Growth and Absent Close to the Melting Level, Journal of Geophysical Research: Atmospheres, 127, e2022JD036 860, https://doi.org/10.1029/2022JD036860, 2022.

Cohen, L. and Dean, S.: Snow on the Ross Ice Shelf: Comparison of Reanalyses and Observations from Automatic Weather Stations, The Cryosphere, 7, 1399–1410, https://doi.org/10.5194/tc-7-1399-2013, 2013.

Coppola, M., Battaglia, A., Tridon, F., and Kollias, P.: Improved Hydrometeor Detection near the Earth's Surface by a Conically Scanning Spaceborne W-Band Radar, Atmospheric Measurement Techniques, 18, 5071–5085, https://doi.org/10.5194/amt-18-5071-2025, 2025.

Corden, H., Delanoë, J., Del Guasta, M., and Berne, A.: Precipitation Processes in an Antarctic Moist Air Intrusion: Insights from Multi-Frequency Radar Observations over a 1100-Km Transect, https://doi.org/10.5194/egusphere-2026-3964, 2026.

Del Guasta, M., Ricaud, P., Scarchilli, C., and Dreossi, G.: A Statistical Study of Precipitation on the Eastern Antarctic Plateau (Dome-C) Using Remote Sensing and in-Situ Instrumentation, Polar Science, 42, https://doi.org/10.1016/j.polar.2024.101106, 2024.

Di Natale, G., Palchetti, L., and Roversi, G.: FIRCLOUDS: Far Infrared Radiative Closure Experiment for Antarctic Clouds – Ground-Based Radar Observations at Concordia Station (Dome C), Dataset, Italian Antarctic Data Center (IANDC), https://iandc.pnra.aq/srv/eng/catalog.search#/metadata/ca61e577-0270-472e-aa4f-6e97c3b1d426, PNRA16_00189/A2; CC BY-NC-SA 4.0, 2018.

Di Natale, G., Turner, D. D., Bianchini, G., Del Guasta, M., Palchetti, L., Bracci, A., Baldini, L., Maestri, T., Cossich, W., Martinazzo, M., and Facheris, L.: Consistency Test of Precipitating Ice Cloud Retrieval Properties Obtained from the Observations of Different Instruments Operating at Dome C (Antarctica), Atmospheric Measurement Techniques, 15, 7235–7258, https://doi.org/10.5194/amt-15-7235-2022, 2022.

https://doi.org/10.5194/egusphere-2026-6639
Preprint. Discussion started: 30 October 2026
© Author(s) 2026. CC BY 4.0 License.

Durán-Alarcón, C., Boudevillain, B., Genthon, C., Grazioli, J., Souverijns, N., van Lipzig, N. P. M., Gorodetskaya, I. V., and Berne, A.: The Vertical Structure of Precipitation at Two Stations in East Antarctica Derived from Micro Rain Radars, The Cryosphere, 13, 247–264, https://doi.org/10.5194/tc-13-247-2019, 2019.

ECMWF: IFS Documentation CY41R2 – Part IV: Physical Processes, ECMWF, Reading, UK, https://doi.org/10.21957/tr5rv27xu, 2016.

Ferrone, A. and Berne, A.: Radar and Ground-Level Measurements of Clouds and Precipitation Collected during the POPE 2020 Campaign at Princess Elisabeth Antarctica, Earth System Science Data, 15, 1115–1132, https://doi.org/10.5194/essd-15-1115-2023, 2023.

Ferrone, A., Vignon, É., Zonato, A., and Berne, A.: Local Spatial Variability in the Occurrence of Summer Precipitation in the Sør Rondane Mountains, Antarctica, The Cryosphere, 17, 4937–4956, https://doi.org/10.5194/tc-17-4937-2023, 2023.

Gehring, J., Vignon, É., Billault-Roux, A.-C., Ferrone, A., Protat, A., Alexander, S. P., and Berne, A.: Orographic Flow Influence on Precipitation During an Atmospheric River Event at Davis, Antarctica, Journal of Geophysical Research: Atmospheres, 127, e2021JD035 210, https://doi.org/10.1029/2021JD035210, 2022.

Genthon, C., Berne, A., Grazioli, J., Durán Alarcón, C., Praz, C., and Boudevillain, B.: Precipitation at Dumont d'Urville, Adélie Land, East Antarctica: The APRES3 Field Campaigns Dataset, Earth System Science Data, 10, 1605–1612, https://doi.org/10.5194/essd-10-1605-2018, 2018.

Gorodetskaya, I., Kneifel, S., Maahn, M., Thiery, W., Schween, J., Mangold, A., Crewell, S., and Van Lipzig, N.: Cloud and Precipitation Properties from Ground-Based Remote-Sensing Instruments in East Antarctica, The Cryosphere, 9, 285–304, https://doi.org/10.5194/tc-9-285-2015, 2015.

Gorodetskaya, I. V., Tsukernik, M., Claes, K., Ralph, M. F., Neff, W. D., and Van Lipzig, N. P. M.: The Role of Atmospheric Rivers in Anomalous Snow Accumulation in East Antarctica, Geophysical Research Letters, 41, 6199–6206, https://doi.org/10.1002/2014GL060881, 2014.

Gossart, A., Souverijns, N., Gorodetskaya, I., Lhermitte, S., Lenaerts, J., Schween, J., Mangold, A., Laffineur, Q., and Van Lipzig, N.: Blowing Snow Detection from Ground-Based Ceilometers: Application to East Antarctica, The Cryosphere, 11, 2755–2772, https://doi.org/10.5194/tc-11-2755-2017, 2017.

Grazioli, J., Madeleine, J.-B., Gallée, H., Forbes, R. M., Genthon, C., Krinner, G., and Berne, A.: Katabatic Winds Diminish Precipitation Contribution to the Antarctic Ice Mass Balance, Proceedings of the National Academy of Sciences, 114, 10 858–10 863, https://doi.org/10.1073/pnas.1707633114, 2017.

Grigioni, P., De Silvestri, L., Ciardini, V., Iaccarino, A., Proposito, M., Camporeale, G., and Scarchilli, C.: ENEIDE Automatic Weather Station Observations at Mario Zucchelli Station (MZS), ENEA Climantartide, https://doi.org/10.12910/DATASET2022-001, 2022a.

Grigioni, P., Iaccarino, A., Ciardini, V., De Silvestri, L., Proposito, M., Camporeale, G., and Scarchilli, C.: CL51 Ceilometer Observations at Mario Zucchelli Station (MZS), ENEA Climantartide, https://doi.org/10.12910/DATASET2022-005, 2022b.

Grigioni, P., Iaccarino, A., Ciardini, V., De Silvestri, L., Proposito, M., Camporeale, G., and Scarchilli, C.: Weather Observations from Radiosonde at Mario Zucchelli Station (MZS), ENEA Climantartide, https://doi.org/10.12910/DATASET2022-003, 2022c.

Hagihara, Y., Okamoto, H., and Yoshida, R.: Development of a Combined CloudSat-CALIPSO Cloud Mask to Show Global Cloud Distribution, Journal of Geophysical Research: Atmospheres, 115, https://doi.org/10.1029/2009JD012344, 2010.

Hersbach, H., Bell, B., Berrisford, P., Hirahara, S., Horányi, A., Muñoz-Sabater, J., Nicolas, J., Peubey, C., Radu, R., Schepers, D., Simmons, A., Soci, C., Abdalla, S., Abellan, X., Balsamo, G., Bechtold, P., Biavati, G., Bidlot, J., Bonavita, M., De Chiara, G., Dahlgren, P., Dee, D., Diamantakis, M., Dragani, R., Flemming, J., Forbes, R., Fuentes, M., Geer, A., Haimberger, L., Healy, S., Hogan, R. J., Hólm, E., Janisková, M., Keeley, S., Laloyaux, P., Lopez, P., Lupu, C., Radnoti, G., de Rosnay, P., Rozum, I., Vamborg, F., Vil-

https://doi.org/10.5194/egusphere-2026-6639
Preprint. Discussion started: 30 October 2026
© Author(s) 2026. CC BY 4.0 License.

laume, S., and Thépaut, J.-N.: The ERA5 Global Reanalysis, Quarterly Journal of the Royal Meteorological Society, 146, 1999–2049, https://doi.org/10.1002/qj.3803, 2020.

Hines, K. M., Rowe, P. M., Gorodetskaya, I. V., Chyhareva, A., Bromwich, D. H., Litell, M. F., Wang, S.-H., Krakovska, S., Durán-Alarcón, C., and Stillwell, R. A.: Skillful Polar WRF Cloud Modeling of a Warm Winter Atmospheric River at the Antarctic Peninsula, Journal of Geophysical Research: Atmospheres, 131, e2024JD043 239, https://doi.org/10.1029/2024JD043239, 2026.

Illingworth, A. J., Battaglia, A., Bradford, J., Forsythe, M., Joe, P., Kollias, P., Lean, K., Lori, M., Mahfouf, J.-F., Melo, S., Midthassel, R., Munro, Y., Nicol, J., Potthast, R., Rennie, M., Stein, T. H. M., Tanelli, S., Tridon, F., Walden, C. J., and Wolde, M.: WIVERN: A New Satellite Concept to Provide Global In-Cloud Winds, Precipitation, and Cloud Properties, Bulletin of the American Meteorological Society, 99, 1669–1687, https://doi.org/10.1175/BAMS-D-16-0047.1, 2018.

IPCC: Climate Change 2021: The Physical Science Basis, Cambridge University Press, https://www.ipcc.ch/report/ar6/wg1/, 2021.

Jakob, F., Radenz, M., Baars, H., Seifert, P., and Engelmann, R.: Continuous Wintertime Water Vapor Profiling by Raman Lidar at Neumayer Station III, Antarctica: Characteristics of Meridional Moisture Transport and Assessment of ERA5 Reanalysis, https://doi.org/10.5194/egusphere-2026-2445, 2026.

Jullien, N., Vignon, É., Sprenger, M., Aemisegger, F., and Berne, A.: Synoptic Conditions and Atmospheric Moisture Pathways Associated with Virga and Precipitation over Coastal Adélie Land in Antarctica, The Cryosphere, 14, 1685–1702, https://doi.org/10.5194/tc-14-1685-2020, 2020.

Kneifel, S. and Moisseev, D.: Long-Term Statistics of Riming in Nonconvective Clouds Derived from Ground-Based Doppler Cloud Radar Observations, Journal of the Atmospheric Sciences, 77, 3495–3508, https://doi.org/10.1175/JAS-D-20-0007.1, 2020.

Knuth, S. L., Tripoli, G. J., Thom, J. E., and Weidner, G. A.: The Influence of Blowing Snow and Precipitation on Snow Depth Change across the Ross Ice Shelf and Ross Sea Regions of Antarctica, Journal of Applied Meteorology and Climatology, 49, 1306–1321, https://doi.org/10.1175/2010JAMC2245.1, 2010.

Kochendorfer, J., Nitu, R., Wolff, M., Mekis, E., Rasmussen, R., Baker, B., Earle, M. E., Reverdin, A., Wong, K., Smith, C. D., Yang, D., Roulet, Y.-A., Buisan, S., Laine, T., Lee, G., Aceituno, J. L. C., Alastrué, J., Isaksen, K., Meyers, T., Brækkan, R., Landolt, S., Jachcik, A., and Poikonen, A.: Analysis of Single-Alter-Shielded and Unshielded Measurements of Mixed and Solid Precipitation from WMO-SPICE, Hydrology and Earth System Sciences, 21, 3525–3542, https://doi.org/10.5194/hess-21-3525-2017, 2017a.

Kochendorfer, J., Rasmussen, R., Wolff, M., Baker, B., Hall, M. E., Meyers, T., Landolt, S., Jachcik, A., Isaksen, K., Brækkan, R., and Leeper, R.: The Quantification and Correction of Wind-Induced Precipitation Measurement Errors, Hydrology and Earth System Sciences, 21, 1973–1989, https://doi.org/10.5194/hess-21-1973-2017, 2017b.

Lamer, K., Kollias, P., Battaglia, A., and Preval, S.: Mind the Gap – Part 1: Accurately Locating Warm Marine Boundary Layer Clouds and Precipitation Using Spaceborne Radars, Atmospheric Measurement Techniques, 13, 2363–2379, https://doi.org/10.5194/amt-13-2363-2020, 2020.

Lauwers, T., Fourré, E., Dutrievoz, N., Agosta, C., Jossoud, O., Minster, B., Prié, F., Cattani, O., Masson-Delmotte, V., Casado, M., Genthon, C., and Landais, A.: Combined and Autonomous Online Measurement of Water Isotopes in Snowflakes and Atmospheric Water Vapor in East Antarctica, Atmospheric Measurement Techniques, 19, 4743–4758, https://doi.org/10.5194/amt-19-4743-2026, 2026.

Lemonnier, F., Madeleine, J.-B., Claud, C., Genthon, C., Durán-Alarcón, C., Palerme, C., Berne, A., Souverijns, N., Van Lipzig, N., Gorodetskaya, I. V., L'Ecuyer, T., and Wood, N.: Evaluation of CloudSat Snowfall Rate Profiles by a Comparison with in Situ Micro-Rain Radar Observations in East Antarctica, The Cryosphere, 13, 943–954, https://doi.org/10.5194/tc-13-943-2019, 2019.

https://doi.org/10.5194/egusphere-2026-6639
Preprint. Discussion started: 30 October 2026
© Author(s) 2026. CC BY 4.0 License.

Liu, Y., Li, F., and Hao, W.: Evaluation of Seasonal and Synoptic Changes in Snow Accumulation in Antarctica between Five Reanalyses Products and in Situ Observations, Atmosphere, 9, https://doi.org/10.3390/atmos9120473, 2018.

Löffler-Mang, M. and Joss, J.: An Optical Disdrometer for Measuring Size and Velocity of Hydrometeors, Journal of Atmospheric and Oceanic Technology, 17, 130–139, https://doi.org/10.1175/1520-0426(2000)017<0130:AODFMS>2.0.CO;2, 2000.

Lubin, D., Zhang, D., Silber, I., Scott, R. C., Kalogeras, P., Battaglia, A., Bromwich, D. H., Cadeddu, M., Eloranta, E., Fridlind, A., Frossard, A., Hines, K. M., Kneifel, S., Leaitch, W. R., Lin, W., Nicolas, J., Powers, H., Quinn, P. K., Rowe, P., Russell, L. M., Sharma, S., Verlinde, J., and Vogelmann, A. M.: AWARE: The Atmospheric Radiation Measurement (ARM) West Antarctic Radiation Experiment, Bulletin of the American Meteorological Society, 101, E1069–E1091, https://doi.org/10.1175/BAMS-D-18-0278.1, 2020.

Maahn, M. and Kollias, P.: Improved Micro Rain Radar Snow Measurements Using Doppler Spectra Post-Processing, Atmospheric Measurement Techniques, 5, 2661–2673, https://doi.org/10.5194/amt-5-2661-2012, 2012.

Maahn, M., Burgard, C., Crewell, S., Gorodetskaya, I. V., Kneifel, S., Lhermitte, S., Van Tricht, K., and van Lipzig, N. P. M.: How Does the Spaceborne Radar Blind Zone Affect Derived Surface Snowfall Statistics in Polar Regions?, Journal of Geophysical Research: Atmospheres, 119, https://doi.org/10.1002/2014JD022079, 2014.

Marchand, R., Mace, G. G., Ackerman, T., and Stephens, G.: Hydrometeor Detection Using Cloudsat—An Earth-Orbiting 94-GHz Cloud Radar, Journal of Atmospheric and Oceanic Technology, 25, 519–533, https://doi.org/10.1175/2007JTECHA1006.1, 2008.

McDonald, A. J., Kuma, P., Panell, M., Petterson, O. K. L., Plank, G. E., Rozliaiani, M. A. H., and Whitehead, L. E.: Evaluating Cloud Properties at Scott Base: Comparing Ceilometer Observations With ERA5, JRA55, and MERRA2 Reanalyses Using an Instrument Simulator, Journal of Geophysical Research: Atmospheres, 130, e2024JD041 754, https://doi.org/10.1029/2024JD041754, 2025.

Milani, L., Kulie, M. S., Casella, D., Dietrich, S., L'Ecuyer, T. S., Panegrossi, G., Porcù, F., Sanò, P., and Wood, N. B.: CloudSat Snowfall Estimates over Antarctica and the Southern Ocean: An Assessment of Independent Retrieval Methodologies and Multi-Year Snowfall Analysis, Atmospheric Research, 213, 121–135, https://doi.org/10.1016/j.atmosres.2018.05.015, 2018.

Nitu, R., Roulet, Y.-A., Wolff, M., Earle, M. E., and Reverdin, A.: WMO Solid Precipitation Intercomparison Experiment (SPICE) (2012 - 2015), Tech. Rep. 131, World Meteorological Organization, https://library.wmo.int/idurl/4/56317, last access: 13 October 2026, 2018.

Okamoto, H., Sato, K., and Hagihara, Y.: Global Analysis of Ice Microphysics from CloudSat and CALIPSO: Incorporation of Specular Reflection in Lidar Signals, Journal of Geophysical Research: Atmospheres, 115, D22 209, https://doi.org/10.1029/2009JD013383, 2010.

Okamoto, H., Sato, K., and Zhang, H.: Analysis of Cloud Properties and Vertical Air Motion by Using EarthCARE Satellite, in: Remote Sensing of Clouds and the Atmosphere XXX, edited by Kassianov, E. I. and Lolli, S., vol. 13668 of *Proceedings of SPIE*, p. 1366808, SPIE, Madrid, Spain, https://doi.org/10.1117/12.3070092, 2025.

Palerme, C., Kay, J. E., Genthon, C., L'Ecuyer, T., Wood, N. B., and Claud, C.: How Much Snow Falls on the Antarctic Ice Sheet?, The Cryosphere, 8, 1577–1587, https://doi.org/10.5194/tc-8-1577-2014, 2014.

Palerme, C., Genthon, C., Claud, C., Kay, J. E., Wood, N. B., and L'Ecuyer, T.: Evaluation of Current and Projected Antarctic Precipitation in CMIP5 Models, Climate Dynamics, 48, 225–239, https://doi.org/10.1007/s00382-016-3071-1, 2017.

Palerme, C., Claud, C., Wood, N. B., L'Ecuyer, T., and Genthon, C.: How Does Ground Clutter Affect CloudSat Snowfall Retrievals Over Ice Sheets?, IEEE Geoscience and Remote Sensing Letters, 16, 342–346, https://doi.org/10.1109/LGRS.2018.2875007, 2019.

Parish, T. R. and Cassano, J. J.: The Role of Katabatic Winds on the Antarctic Surface Wind Regime, Monthly Weather Review, 131, 317–333, https://doi.org/10.1175/1520-0493(2003)131<0317:TROKWO>2.0.CO;2, 2003.

Peters, G., Fischer, B., and Andersson, T.: Rain Observations with a Vertically Looking Micro Rain Radar (MRR), Boreal Environment Research, 7, 353–362, https://www.borenv.net/BER/archive/pdfs/ber7/ber7-353.pdf, last access: 13 October 2026, 2002.

https://doi.org/10.5194/egusphere-2026-6639
Preprint. Discussion started: 30 October 2026
© Author(s) 2026. CC BY 4.0 License.

Petteni, A., Casado, M., Leroy-Dos Santos, C., Landais, A., Dutrievoz, N., Agosta, C., Akers, P. D., Savarino, J., Spolaor, A., Frezzotti, M., and Stenni, B.: Air Mass Origin and Local Impacts on Antarctic Snow Isotopic Composition: An Observation and Modelling Study, The Cryosphere, 20, 3581–3598, https://doi.org/10.5194/tc-20-3581-2026, 2026.

Protat, A., Bouniol, D., Delanoë, J., O'Connor, E., May, P. T., Plana-Fattori, A., Hasson, A., Görsdorf, U., and Heymsfield, A. J.: Assessment of Cloudsat Reflectivity Measurements and Ice Cloud Properties Using Ground-Based and Airborne Cloud Radar Observations, Journal of Atmospheric and Oceanic Technology, 26, 1717–1741, https://doi.org/10.1175/2009JTECHA1246.1, 2009.

Radenz, M., Engelmann, R., Henning, S., Schmithüsen, H., Baars, H., Frey, M. M., Weller, R., Bühl, J., Jimenez, C., Roschke, J., Muser, L. O., Wullenweber, N., Zeppenfeld, S., Griesche, H., Wandinger, U., and Seifert, P.: Ground-Based Remote Sensing of Aerosol, Clouds, Dynamics, and Precipitation in Antarctica: First Results from the 1-Year COALA Campaign at Neumayer Station III in 2023, Bulletin of the American Meteorological Society, 105, E1438–E1457, https://doi.org/10.1175/BAMS-D-22-0285.1, 2024.

Rasmussen, R. M., Hallett, J., Purcell, R., Landolt, S. D., and Cole, J.: The Hotplate Precipitation Gauge, Journal of Atmospheric and Oceanic Technology, 28, 148–164, https://doi.org/10.1175/2010JTECHA1375.1, 2011.

Roussel, M.-L., Wiener, V., Genthon, C., Vignon, E., Bazile, E., Agosta, C., Berne, A., Durán-Alarcón, C., Dufresne, J.-L., and Claud, C.: Assessing the Simulation of Snowfall at Dumont d'Urville, Antarctica, during the YOPP-SH Special Observing Campaign, Quarterly Journal of the Royal Meteorological Society, 149, 1391–1406, https://doi.org/10.1002/qj.4463, 2023.

Roversi, G.: snowreach: Virga Classification and Blind-Zone Simulation for Vertically Pointing Radars, Zenodo, https://doi.org/10.5281/ZENODO.23087597, v1.0.2, 2026.

Roversi, G., Bracci, A., and Baldini, L.: Particle Size and Velocity Distributions from an OTT Parsivel Optical Disdrometer Located at Mario Zucchelli Station, Aggregated to 5min, Monthly netCDF Archive, https://doi.org/10.5281/ZENODO.22922844, v1.0.2, 2026a.

Roversi, G., Bracci, A., and Baldini, L.: Vertically Pointing Doppler Radar Profiles (24 GHz Metek MRR-2) at Mario Zucchelli Station (Terra Nova Bay, Antarctica), Aggregated to 5min, Monthly netCDF Archive, https://doi.org/10.5281/ZENODO.22923006, v1.0.2, 2026b.

Roversi, G., Bracci, A., Sato, K., Okamoto, H., and Baldini, L.: Four Years of Vertically Pointing Radar Observations at Mario Zucchelli Station, Antarctica, and Implications for Satellite Ground Validation, in: Proc. URSI GASS, 2026c.

Saini, L., Das, S., and Murukesh, N.: Case Studies of Different Types of Precipitation at Ny-Ålesund, Arctic, Scientific Reports, 15, 3086, https://doi.org/10.1038/s41598-025-85833-2, 2025.

Saini, L., Das, S., and Murukesh, N.: Development of a Virga Detection Tool and Associated Study of Arctic Virga and Precipitation, Journal of Geophysical Research: Atmospheres, 131, e2025JD044 204, https://doi.org/10.1029/2025JD044204, 2026a.

Saini, L., Das, S., and Murukesh, N.: Vertical Evolution of Precipitation and Associated Atmospheric Parameters at Ny-Ålesund (78°55′N, 11°56′E) in the Arctic, Atmospheric Research, 329, 108 531, https://doi.org/10.1016/j.atmosres.2025.108531, 2026b.

Sato, K. and Okamoto, H.: Refinement of Global Ice Microphysics Using Spaceborne Active Sensors, Journal of Geophysical Research, 116, D20 202, https://doi.org/10.1029/2011JD015885, 2011.

Sato, K. and Okamoto, H.: Global Analysis of Height-Resolved Ice Particle Categories From Spaceborne Lidar, Geophysical Research Letters, 50, e2023GL105 522, https://doi.org/10.1029/2023GL105522, 2023.

Sato, K. and Okamoto, H.: EarthCARE L2 Cloud-Precipitation and Vertical Velocity Products, in: Remote Sensing of Clouds and the Atmosphere XXX, edited by Kassianov, E. I. and Lolli, S., vol. 13668 of *Proceedings of SPIE*, p. 1366815, SPIE, Madrid, Spain, https://doi.org/10.1117/12.3070102, 2025.

https://doi.org/10.5194/egusphere-2026-6639
Preprint. Discussion started: 30 October 2026
© Author(s) 2026. CC BY 4.0 License.

Sato, K., Okamoto, H., Nishizawa, T., Jin, Y., Nakajima, T. Y., Wang, M., Satoh, M., Roh, W., Ishimoto, H., and Kudo, R.: JAXA Level 2 Cloud and Precipitation Microphysics Retrievals Based on EarthCARE Radar, Lidar, and Imager: The CPR_CLP, AC_CLP, and ACM_CLP Products, Atmospheric Measurement Techniques, 18, 1325–1338, https://doi.org/10.5194/amt-18-1325-2025, 2025.

Scarchilli, C., Ciardini, V., Grigioni, P., Iaccarino, A., De Silvestri, L., Proposito, M., Dolci, S., Camporeale, G., Schioppo, R., Antonelli, A., Baldini, L., Roberto, N., Argentini, S., Bracci, A., and Frezzotti, M.: Characterization of Snowfall Estimated by in Situ and Ground-Based Remote-Sensing Observations at Terra Nova Bay, Victoria Land, Antarctica, Journal of Glaciology, 66, 1006–1023, https://doi.org/10.1017/jog.2020.70, 2020.

Scarsi, F. E., Battaglia, A., Maahn, M., and Lhermitte, S.: How to Reduce Sampling Errors in Spaceborne Cloud Radar-Based Snowfall Estimates, The Cryosphere, 19, 4875–4892, https://doi.org/10.5194/tc-19-4875-2025, 2025.

Schmale, J., Aemisegger, F., Berne, A., Creamean, J., et al.: Antarctica InSync Scientific Theme 6. Aerosol-Cloud-Precipitation Interactions and Radiative Feedbacks. Scientific Committee on Antarctic Research (SCAR), Tech. rep., Scientific Committee on Antarctic Research, https://doi.org/10.67382/XXZE4220, 2026.

Schmithüsen, H.: Ceilometer Raw Data Measured at Neumayer Station (2009-02 et Seq), https://doi.org/10.1594/PANGAEA.952482, 2022.

Schmithüsen, H.: Micro Rain Radar (MRR) Raw Data Measured at Neumayer Station (2019-01 et Seq), https://doi.org/10.1594/PANGAEA.981119, 2025.

Seefeldt, M. W., Low, T. M., Landolt, S. D., and Nylen, T. H.: Remote and Autonomous Measurements of Precipitation for the Northwestern Ross Ice Shelf, Antarctica, Earth System Science Data, 13, 5803–5817, https://doi.org/10.5194/essd-13-5803-2021, 2021.

Shates, J. A., Pettersen, C., L'Ecuyer, T. S., and Kulie, M. S.: KAZR-CloudSat Analysis of Snowing Profiles at the North Slope of Alaska: Implications of the Satellite Radar Blind Zone, Journal of Geophysical Research: Atmospheres, 130, e2024JD042 700, https://doi.org/10.1029/2024JD042700, 2025.

Song, V., Yang, Y., and Bhatta, S.: Antarctic Snowfall Patterns and Trends: A Regional Analysis Across Multiple Data Sets, Earth and Space Science, 13, e2025EA004 834, https://doi.org/10.1029/2025EA004834, 2026.

Souverijns, N., Gossart, A., Lhermitte, S., Gorodetskaya, I., Kneifel, S., Maahn, M., Bliven, F., and Van Lipzig, N.: Estimating Radar Reflectivity - Snowfall Rate Relationships and Their Uncertainties over Antarctica by Combining Disdrometer and Radar Observations, Atmospheric Research, 196, 211–223, https://doi.org/10.1016/j.atmosres.2017.06.001, 2017.

Souverijns, N., Gossart, A., Lhermitte, S., Gorodetskaya, I. V., Grazioli, J., Berne, A., Duran-Alarcon, C., Boudevillain, B., Genthon, C., Scarchilli, C., and van Lipzig, N. P. M.: Evaluation of the CloudSat Surface Snowfall Product over Antarctica Using Ground-Based Precipitation Radars, The Cryosphere, 12, 3775–3789, https://doi.org/10.5194/tc-12-3775-2018, 2018.

Sun, J., Lv, J., Li, H., Zhang, W., Tian, B., and Ding, M.: Brief Communication: Two-Year MRR Observations at Great Wall Station, Antarctic Peninsula Region, The Cryosphere, 20, 4049–4059, https://doi.org/10.5194/tc-20-4049-2026, 2026.

Tokay, A., Wolff, D. B., and Petersen, W. A.: Evaluation of the New Version of the Laser-Optical Disdrometer, OTT Parsivel2, Journal of Atmospheric and Oceanic Technology, 31, 1276–1288, https://doi.org/10.1175/JTECH-D-13-00174.1, 2014.

Tridon, F., Silber, I., Battaglia, A., Kneifel, S., Fridlind, A., Kalogeras, P., and Dhillon, R.: Highly Supercooled Riming and Unusual Triple-Frequency Radar Signatures over McMurdo Station, Antarctica, Atmospheric Chemistry and Physics, 22, 12 467–12 491, https://doi.org/10.5194/acp-22-12467-2022, 2022.

Vaisala Oyj: CL51 Technical Description, Tech. Rep. M212735EN-A, Vaisala Oyj, Helsinki, Finland, https://docs.vaisala.com/r/M212735EN-A/en-US, last access: 16 September 2026, 2024.

https://doi.org/10.5194/egusphere-2026-6639
Preprint. Discussion started: 30 October 2026
© Author(s) 2026. CC BY 4.0 License.

Vaisala Oyj: CL51 User Guide, Tech. Rep. M210801EN-K, Vaisala Oyj, Helsinki, Finland, https://docs.vaisala.com/r/M210801EN-K/en-US, last access: 16 September 2026, 2025.

Valdivia, J. M., Gatlin, P. N., Kumar, S., Scipión, D., Silva, Y., and Petersen, W. A.: The GPM-DPR Blind Zone Effect on Satellite-Based Radar Estimation of Precipitation over the Andes from a Ground-Based Ka-Band Profiler Perspective, Journal of Applied Meteorology and Climatology, 61, 441–456, https://doi.org/10.1175/JAMC-D-20-0211.1, 2022.

Wang, Y., You, Y., and Kulie, M.: Global Virga Precipitation Distribution Derived From Three Spaceborne Radars and Its Contribution to the False Radiometer Precipitation Detection, Geophysical Research Letters, 45, 4446–4455, https://doi.org/10.1029/2018GL077891, 2018.

Wehr, T., Kubota, T., Tzeremes, G., Wallace, K., Nakatsuka, H., Ohno, Y., Koopman, R., Rusli, S., Kikuchi, M., Eisinger, M., Tanaka, T., Taga, M., Deghaye, P., Tomita, E., and Bernaerts, D.: The EarthCARE Mission – Science and System Overview, Atmospheric Measurement Techniques, 16, 3581–3608, https://doi.org/10.5194/amt-16-3581-2023, 2023.

Wiener, V., Roussel, M.-L., Genthon, C., Vignon, É., Grazioli, J., and Berne, A.: A 7-Year Record of Vertical Profiles of Radar Measurements and Precipitation Estimates at Dumont d'Urville, Adélie Land, East Antarctica, Earth System Science Data, 16, 821–836, https://doi.org/10.5194/essd-16-821-2024, 2024.

Yuter, S. E. and Houze, R. A.: Three-Dimensional Kinematic and Microphysical Evolution of Florida Cumulonimbus. Part II: Frequency Distributions of Vertical Velocity, Reflectivity, and Differential Reflectivity, Monthly Weather Review, 123, 1941–1963, https://doi.org/10.1175/1520-0493(1995)123<1941:TDKAME>2.0.CO;2, 1995.

Zelasko, N., Wettlaufer, A., Borkhuu, B., Burkhart, M., Campbell, L. S., Steenburgh, W. J., and Snider, J. R.: Hotplate Precipitation Gauge Calibrations and Field Measurements, Atmospheric Measurement Techniques, 11, 441–458, https://doi.org/10.5194/amt-11-441-2018, 2018.